

Physicochemical models of formation of gold–silver mineralization at the Rogovik deposit (Northeastern Russia)



T.V. Zhuravkova^{a,b,*}, G.A. Palyanova^{a,b}, K.V. Chudnenko^c, R.G. Kravtsova^c, I.R. Prokopyev^{a,b}, A.S. Makshakov^c, A.S. Borisenko^{a,b}

^a Sobolev Institute of Geology and Mineralogy, Siberian Branch Russian Academy of Sciences, pr. Akademika Koptyuga, 3, Novosibirsk 630090, Russia

^b Novosibirsk State University, Pirogova str., 1, Novosibirsk 630090, Russia

^c Vinogradov Institute of Geochemistry, Siberian Branch of the RAS, Favorskogo str., 1a, Irkutsk 664033, Russia

ARTICLE INFO

Keywords:

Fluid inclusions study
Thermodynamic modeling
Gold
Silver
Au-Ag amalgams
Rogovik deposit

ABSTRACT

The T,X-parameters of the main ore-forming stages of the Rogovik epithermal gold-silver deposit (northeastern Russia) were determined using microthermometric techniques on fluid inclusion assemblages. On the basis of these data we carried out thermodynamic calculations that model the formation conditions of three types of ore mineral assemblages: gold-silver – at the early volcanic stage, silver-polymetallic and silver-gold-polymetallic – at the late volcanoplutonic stage. The silver-gold-polymetallic mineralization is located at the sites where silver-polymetallic and gold-silver zones overlap. The calculations were made using the “Selektor-C” software within a complex geochemical multicomponent system. Several scenarios of formation of gold-silver mineralization at an early volcanic stage were considered: 1) boiling of a hydrothermal solution; 2) interaction of residual aqueous solution with host rocks; 3) mixing of an ore-bearing gas phase with meteoric waters. For the late volcanoplutonic stage, we modeled formation of “silver mineralization” using an ore-forming solution genetically related to a deep-seated granite massif and its interaction with host rocks and gold-silver zones of early volcanic stage. These physicochemical models substantially improve our understanding of formation of the three types of mineral assemblages at the Rogovik deposit and can be applied to other epithermal deposits with similar mineralization styles.

1. Introduction

The Rogovik epithermal gold-silver (Au-Ag) deposit (Fig. 1a) is located in the Omsukchan ore district in northeastern Russia, one of the richest in terms of gold and silver endowment (Sidorov, 1987). In addition to Au-Ag deposits (Dukat, Arylakh, Primorskoe, Lunnoe and Rogovik), there are also silver-polymetallic (Gol'tsovoe, Tedit and Mechta) and tin-silver (Novo-Dzhaginskoe, Valunnoe and Malokenskoe) deposits (Kalinin et al., 1984; Konstantinov et al., 1998, 2003; Kravtsova, 2010; Kravtsova et al., 1998, 2012, 2015; Kuznetsov et al., 1992; Plyashkevich, 2002; Ryzhov et al., 2000). The Rogovik deposit has a complex mineralogical composition and was formed by at least two separate events (Kravtsova et al., 2012, 2015). Three types of mineral assemblages were described: gold-silver (Au-Ag), silver-polymetallic (Ag-Pb) and silver-gold-polymetallic (Ag-Au-Pb). They were formed during two major stages. Formation of the Au-Ag mineralization is related to the early volcanic stage, while Ag-Pb and Ag-Au-Pb mineralization is related to the late volcanoplutonic stage. During the late

volcanoplutonic stage, simultaneously with the Ag-Pb mineralized zone, at the sites of overlapping Ag-Pb with Au-Ag mineralization, there are Ag-Au-Pb mineralized zones of complex composition (Kravtsova et al., 2015; Pal'yanova et al., 2015; Zhuravkova et al., 2015).

The aim of this study is to conduct a detailed analysis of chemical composition of major ore minerals, to determine the T,X-parameters of main ore-forming stages, using fluid inclusions and model the physicochemical conditions of ore formation at the Rogovik epithermal Au-Ag deposit. The samples were studied using reflected light and scanning electron microscopy, fluid inclusions microthermometry and Raman spectroscopy. Modeling of chemical mass transfer in geochemical processes was carried out using the “Selektor-C” software, in which the convex programming minimization of Gibbs energy method was applied (Karpov et al., 1997, 2002; Chudnenko, 2010). The subregular and regular activity models for Ag₂(S,Se) (Pal'yanova et al., 2014) and Ag-Au-Hg (Chudnenko and Pal'yanova, 2013) solid solutions were used in the thermodynamic simulations (Chudnenko et al., 2015; Chudnenko and Palyanova, 2016).

* Corresponding author.

E-mail address: zhur0502@rambler.ru (T.V. Zhuravkova).

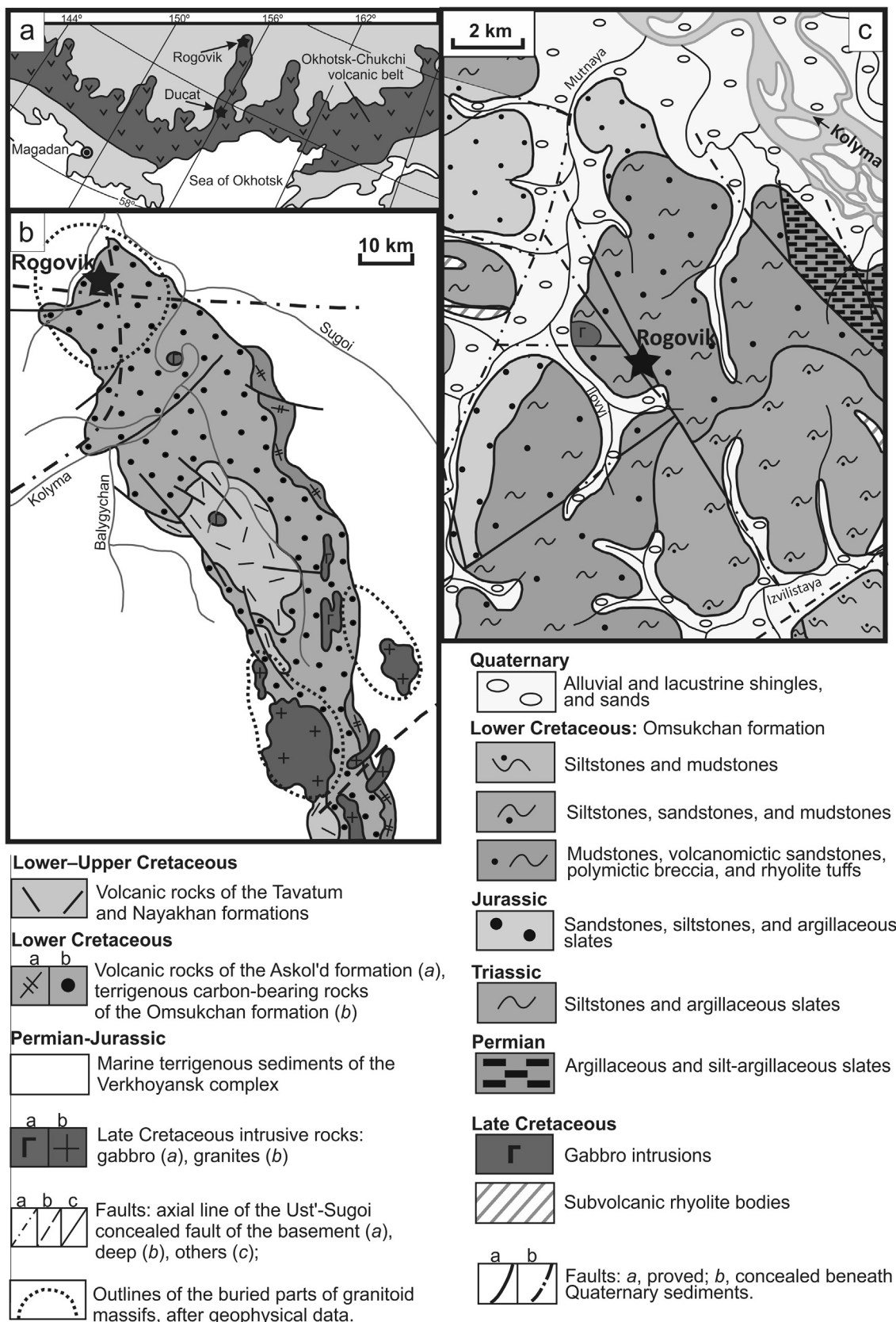


Fig. 1. Map of the Rogovik deposit: (a) Location of the Rogovik deposit in the Okhotsk-Chukchi volcanic belt. (b) Structure of the northern flank of the Balygychan–Sugoi trough modified from Kuznetsov and Livach (2005); (c) Geological sketch map (modified from Kravtsova et al., 2015).

We adhere to the terminology used in our previous works (Pal'yanova and Kolonin, 2007 and references cited therein): “native silver” – $\text{Ag}_{1.0}\text{Au}_{0.0}$ – $\text{Ag}_{0.94}\text{Au}_{0.06}$ (0–100%), “kustelite” – $\text{Ag}_{0.94}\text{Au}_{0.06}$ – $\text{Ag}_{0.85}\text{Au}_{0.15}$ (100–250%), “electrum” – $\text{Ag}_{0.85}\text{Au}_{0.15}$ – $\text{Ag}_{0.44}\text{Au}_{0.56}$ (250–700%); “high-fineness gold” – $\text{Ag}_{0.44}\text{Au}_{0.56}$ – $\text{Ag}_{0.0}\text{Au}_{1.0}$ (700–1000%). As for native silver and gold containing mercury, we use “silver and/or gold amalgams” concerning binary and ternary natural solid solutions and stoichiometric compounds of silver and/or gold with mercury or Hg-rich high-fineness gold, electrum, kustelite and silver.

The combination of detailed mineralogical study and microthermometry on fluid inclusions determining the P,T,X-parameters of ore forming processes with numerical simulations of potential ore forming processes is crucial to understand the controlling factors of ore formation at the Rogovik deposit. Many Au-Ag ore deposits show similarity in mineralogy. It is possible that ore formation processes have very complicated mineralogy with multiple overlapping stages of ore formation, which cover long periods of time and different magmatic-epithermal events. The systematic approach employed in this study is relevant to other deposits with similar mineralization styles and will find application to improve exploration success and considerably increase the efficiency of prospecting.

2. Methodology

2.1. Field sampling

Field work was carried out from July to August 2011 at the Rogovik deposit. To study the petrographic and mineral composition of rocks and ores, we collected 316 samples from drill core and prepared 108 thin sections and 86 polished sections. Geochemical samples, 400–500 g in weight, were crushed to a grain size of < 0.3 mm. For this purpose we used a conventional mechanical jaw crusher. Sample control was made by approximate quantitative atomic-emission spectral analysis (AQAESA) for 50 chemical elements. The atomic-absorption method was used to determine Au and Hg. Lumps of ores were crushed to < 2 mm, which were scattered on mineralogical sieves into fractions of 1–2 mm, 0.5–1 mm, 0.25–0.5 mm and < 0.25 mm, elutriated and their mineral compositions were studied.

2.2. Mineral analyses

Mineral phases were identified and described using optical and scanning electron microscopy, and the composition was determined by electron probe microanalysis (EPMA), using a JXA-8200 (JEOL Ltd, Japan) microprobe (Institute of Geochemistry, Irkutsk, Russia, analyst L.A. Pavlova) and a MIRA 3 LMU (Tescan Orsay Holding) with EDS INCA Energy 450+ (Analytical Center for Multielement and Isotope Research, Siberian Branch, Russian Academy of Sciences, Novosibirsk, Russia, analyst N.S. Karmanov).

A JXA-8200 microprobe supplied with energy dispersive and wave-dispersive spectrometers (WDS) was used. The spectra of the analytical lines of the elements to be analyzed were recorded at an accelerating voltage of 20 kV, beam current of 20 nA, beam diameter of 1 μm , and exposure time of 30 s. Analyses on MIRA 3 LMU (with the use of SEM-EDS in most cases) were performed at 20 kV accelerating voltage and 1.5 nA probe current, the counting time was 15–20 s. Acquisition of spectra was performed in the raster mode with the scanning area from $0.5 \times 0.5 \mu\text{m}^2$ for fine phases and to $2 \times 2 \mu\text{m}^2$ for larger phases, with a slightly defocused electron beam. We analyzed mainly coarse grains (> 10 μm) to prevent contamination of elements from the surrounding phases. Under these analytical conditions, the detection limits of elements were < 0.1%. The uncertainty was $\leq 1\%$ for major components (> 10–15 wt%) and < 2% for minor ones (1–10 wt%). Standardization was done on well-characterized metals (Au, Ag, Au-Ag alloys), chalcogenides (FeS_2 , ZnS , CuFeS_2 , PbSe , etc.) and oxides (Fe_2O_3 , etc.).

2.3. Fluid inclusions study

To obtain information on the T,X-parameters of the main stages of mineral formation, we prepared and studied a double-polished thin section containing fluid inclusions of required size and suitable for analyses. Phase proportions, sizes and shapes of inclusions were studied using an “Olympus BX51” microscope with attached camera adapter. Homogenization temperatures (vapor disappearance, T_h ; CO_2 meniscus disappearance, T_{h,CO_2}), final melting temperatures of clathrates (the melting point of clathrate for fluid inclusions containing liquid CO_2 , $T_{m,\text{Clr}}$), final ice melting temperatures (the melting point of the last ice crystal, T_m) and eutectics temperatures (temperature of the lowest melting point, T_{eut}) were obtained using a Linkam THMSG–600 heating-freezing stage with a precision of ± 0.1 °C in the temperature range of –20 to +80 °C and ± 1 °C beyond this interval. Calibration of the Linkam THMSG–600 heating-freezing stage was performed using natural fluid inclusions with pure CO_2 and inorganic compounds with known temperatures of phase transitions. Salt composition of the solutions from fluid inclusions was determined using the diagrams of two- and three-component water-salt solutions (Borisenko, 1977; Roedder, 1984). Raman spectrometry and microthermometry were used to determine the major composition of fluid inclusions. The salinity is expressed in wt% NaCl equivalent (NaCl-eq., %) and was calculated from microthermometric data using the Flincor program (Brown, 1989). Compositions of gas mixtures (CH_4 , CO_2 , H_2) and solid phases in fluid inclusions were determined by Raman analyses on a Ramanor U–1000 spectrometer, with detector Horiba DU420E–OE–323 of JobinYvon and with laser MillenniaPro of Spectra–Physics. The spectra were calibrated against the emission lines of a standard neon lamp and the peak positions were accurate to $\pm 0.2 \text{ cm}^{-1}$. Molar proportion of gaseous mixtures was calculated from Raman data, using equations from Frezzotti et al. (2012). All microanalytical studies of fluid inclusions were carried out at the Analytical Center for Multielemental and Isotope Research, Siberian Branch, Russian Academy of Sciences, Novosibirsk, Russia.

2.4. Thermodynamic modeling

To perform thermodynamic calculations, we used the «Selektor-C» software (Chudnenko, 2010) based on convex programming. This software includes an algorithm for calculating rock and heterogeneous fluid equilibria in multi-element and multi-phase systems for different T,P-conditions with implementation of solid solution models. Redistribution of substance between different systems (rocks) is considered according to the specified scenario of external and internal flows consisting of a group of mobile phases (water, gases, etc).

Modeling was carried out for the system Na–K–Mg–Ca–Al–Si–Ti–Mn–Fe–Cu–Zn–Pb–Ag–Au–Hg–As–Sb–S–Se–Cl–C–H–O at temperatures of 25–300 °C and pressures of 1–100 bar. Tables 1–3 summarize all phases considered in the model and contain sources of thermodynamic data for all minerals, aqueous complexes, gases and gaseous species. Some gas complexes of gold and silver and solid solutions Au-Ag-Hg and $\text{Ag}_2\text{S}_{1-x}\text{Se}_x$ ($0 \leq x \leq 1$) were added to the “Selektor-C” database in adapted form. In the calculations we used thermodynamic properties of aqueous selenium species ($\text{H}_2\text{SeO}_{3\text{aq}}$, HSeO_3^- , HSeO_4^- , SeO_3^{2-} , SeO_4^{2-}) from Johnson et al. (1992). The constants for HSe^- and dissolved hydroselenide silver complexes (AgHSe_{aq} , $\text{Ag}(\text{HSe})_2^-$) were taken from Akinfiev and Tagirov (2006). The thermodynamic parameters (Gibbs energy, entropy and coefficients of the heat capacity equation) for most gaseous species of selenium are taken from the database of Yokokawa (1988). Data for H_2Se_g were introduced from Akinfiev and Tagirov (2006). Hydrated gas complexes, such as $\text{AgCl}(\text{H}_2\text{O})_n$, $\text{AuCl}(\text{H}_2\text{O})_n$, $\text{AuS}(\text{H}_2\text{O})_n$, $\text{AuS}(\text{H}_2\text{S})(\text{H}_2\text{O})_n$, with hydration numbers (n) of 1–4 (Akinfiev and Zotov, 2016; Hurtig and Williams-Jones, 2014, 2015), were also used in the calculations. Thermodynamic properties of Au-Ag-Hg and Ag-S-Se solid solutions were taken from Chudnenko and Pal'yanova, 2013 and Pal'yanova et al. (2014).

Table 1
Components of aqueous solutions and sources of their thermodynamic data.

Component	Ref	Component	Ref	Component	Ref	Component	Ref
Ag ⁺	1	Cu ⁺	2	HSe ⁻	5	Mn ²⁺	2
Ag ²⁺	1	Cu ²⁺	1	H ₂ SeO _{3aq}	6	Mn ³⁺	2
AgO ⁻	2	CuO _{aq}	2	HSeO _{3⁻}	6	MnO _{aq}	2
AgOH _{aq}	3	CuO _{2²⁻}	2	HSeO _{4⁻}	6	MnO _{2²⁻}	2
Ag(OH) _{2⁻}	3	CuOH _{aq}	3	H ₂ Sb ₂ S _{4aq}	11	MnO _{4⁻}	2
AgCl _{aq}	3	CuOH ⁺	2	HSb ₂ S _{4⁻}	11	MnO _{4²⁻}	2
AgCl _{2⁻}	3	Cu(OH) _{2⁻}	3	HSbO _{2aq}	2	MnOH ⁺	2
Ag(CO ₃) ⁻	4	CuCl _{aq}	3	H ₄ SiO _{4aq}	4	MnCl ⁺	4
Ag(CO ₃) _{2³⁻}	4	CuCl ⁺	4	HSiO _{3⁻}	4	MnSO _{4aq}	4
AgHS _{aq}	3	CuCl _{2aq}	4	HCO _{3⁻}	2	Na ⁺	2
Ag(HS) _{2⁻}	3	CuCl _{2⁻}	3	HCl _{aq}	6	NaOH _{aq}	2
AgHSe _{aq}	5	CuCl _{3⁻}	4	HFeO _{2aq}	2	NaCl _{aq}	4
Ag(HSe) _{2⁻}	5	CuCl _{4²⁻}	4	HFeO _{2⁻}	2	NaH ₂ AsO _{3aq}	10
Al ³⁺	6	CuH ₂ AsO _{3⁺}	10	HHgO _{2⁻}	2	NaH ₂ AsO _{4aq}	10
Al(OH) ²⁺	6	CuH ₂ AsO _{4⁺}	10	HMnO _{2⁻}	2	NaHASO _{4⁻}	10
Al(OH) _{2⁺}	7	CuHASO _{4aq}	10	Hg ²⁺	2	NaHSiO _{3aq}	4
Al(OH) _{3aq}	8	CuAsO _{4⁻}	10	Hg _{2²⁺}	2	NaSO _{4⁻}	6
Al(OH) _{4⁻}	8	CuHS _{aq}	3	HgO _{aq}	2	Pb ²⁺	2
As(OH) _{3aq}	9	Cu(HS) _{2⁻}	3	Hg(OH) _{2aq}	11	PbO _{aq}	2
AsO(OH) _{3aq}	9	Fe ²⁺	2	HgOH ⁺	2	PbOH ⁺	2
AsO _{2⁻}	2	Fe ³⁺	2	HgCl ⁺	4	PbCl ⁺	4
AsO _{4³⁻}	2	FeO _{aq}	2	HgCl ₂	4	PbCl _{2aq}	4
Au ⁺	3	FeO ⁺	2	HgCl _{3⁻}	4	PbCl _{3⁻}	4
Au ³⁺	2	FeO _{2⁻}	2	HgCl _{4²⁻}	4	PbCl _{4⁻}	4
AuOH _{aq}	3	FeOH ⁺	2	Hg(HS) _{2aq}	11	PbH ₂ AsO _{3⁺}	10
Au(OH) _{2⁻}	3	FeOH ²⁺	2	HgS(HS) ⁻	11	PbH ₂ AsO _{4⁺}	10
AuCl _{aq}	3	FeCl _{2aq}	4	K ⁺	2	PbHASO _{4aq}	10
AuCl _{2⁻}	3	FeCl ⁺	4	KOH _{aq}	2	PbAsO _{4⁻}	10
AuHS _{aq}	3	FeCl ²⁺	4	KCl _{aq}	4	Pb(HS) _{2aq}	4
Au(HS) _{2⁻}	3	FeHASO _{4aq}	10	KHSO _{4aq}	4	Pb(HS) _{3⁻}	4
CO _{aq}	6	FeHASO _{4⁺}	10	KSO _{4⁻}	4	SO _{4²⁻}	2
CO _{2aq}	6	FeH ₂ AsO _{3²⁺}	10	KH ₂ AsO _{4aq}	10	SeO _{3²⁻}	6
CO _{3²⁻}	2	FeH ₂ AsO _{4⁺}	10	KHASO _{4⁻}	10	SeO _{4²⁻}	6
Ca ²⁺	2	FeH ₂ AsO _{4²⁺}	10	CH _{4aq}	6	Sb(OH) _{3aq}	11
CaOH ⁺	2	FeAsO _{4aq}	10	H _{2aq}	2	Sb(OH) _{4⁻}	11
CaHCO _{3⁺}	2	FeAsO _{4⁻}	10	O _{2aq}	2	Sb ₂ S _{4²⁻}	11
CaCO _{3aq}	4	H ₃ As ₃ S _{6aq}	11	Mg ²⁺	2	SbO _{2⁻}	2
CaCl ⁺	4	H ₂ As ₃ S ₆	11	MgOH ⁺	2	SiO _{2aq}	6
CaCl _{2aq}	4	HAS ₃ S _{6²⁻}	11	MgCl ⁺	4	Zn ²⁺	2
CaAsO _{4⁻}	10	H ₂ AsO _{3⁻}	11	MgCO _{3aq}	4	ZnO _{aq}	2
CaHASO _{4aq}	10	H ₂ AsO _{4⁻}	2	MgSO _{4aq}	6	ZnO _{2²⁻}	2
CaH ₂ AsO _{3⁺}	10	HASO _{4²⁻}	2	MgH ₂ AsO _{3⁺}	10	ZnOH ⁺	2
CaH ₂ AsO _{4⁺}	10	HASO _{2aq}	2	MgH ₂ AsO _{4⁺}	10	ZnCl ⁺	4
CaHSiO _{3⁺}	4	H ₂ S _{aq}	11	MgHASO _{4aq}	10	ZnCl _{2aq}	4
CaSO _{4aq}	4	HS ⁻	11	MgAsO _{4⁻}	10	ZnCl _{3⁻}	4
Cl ⁻	2	HSO _{4⁻}	2	MgHSiO _{3⁺}	4		

References: 1 – Shock et al. (1989); 2 – Shock et al. (1997); 3 – Akinfiev and Zotov, (2001); 4 – Sverjensky et al. (1997); 5 – Akinfiev and Tagirov (2006); 6 – Johnson et al. (1992); 7 – Pokrovski and Helgeson (1995); 8 – Diakonov et al. (1996); 9 – Perfetti et al. (2008); 10 – Marini and Accornero (2012); 11 – Bessinger and Apps (2003).

Activity coefficients for solid solutions of carbonates (calcite, siderite, magnesite, rhodochrosite), micas (muscovite, paragonite, celadonite, Fe-celadonite), chlorites (clinocllore, daphnite, amesite, Al-free-chlorite), plagioclases (albite, anorthite) and Kfs (microcline, sanidine) are calculated using the non-ideal models of solid solutions considered in Holland et al. (1998) and Holland and Powell (1998, 2003). Calculation of the Gibbs free energy for aqueous solution components was performed using the modified HKF equation (Tanger and Helgeson, 1988). Partial boiling of hydrothermal solution was modeled at pressure drop to the pressure of saturated vapor. Thermodynamic properties (Gibbs free energy, entropy, heat capacity) for vapor and liquid of water were calculated following (Haar et al., 1984).

Estimation of the saturated vapor pressure at a given temperature for all gases was calculated from the Lee-Kesler method (Lee and Kesler, 1975). In the region of high pressures, deviation from the ideal mixture of real gases is calculated using Van-der-Waals equation in the modification of D. Bertole (Walas, 1985) and (Breedveld and Prausnitz, 1973). Fugacity coefficients and molar volumes of gases were

Table 2
Main gases and gas complexes of sulfur, selenium, stibium, silver, gold, mercury and sources of their thermodynamic data.

Component	Ref	Component	Ref	Component	Ref
Ag	1	CH ₄	5	SO ₂	5
Ag ₂	1	CO	5	SO ₃	5
AgCl	2	CO ₂	5	S ₂ O	1
AgCl(H ₂ O)	2	Cl	1	SCL	1
AgCl(H ₂ O) ₂	2	Cl ₂	5	SCL ₂	1
AgCl(H ₂ O) ₃	2	ClO	1	S ₂ Cl	1
AgCl(H ₂ O) ₄	2	ClO ₂	1	S ₂ Cl ₂	1
AgS	1	Cl ₂ O	1	Sb	1
As	1	Cu	1	Sb ₂	1
As ₂	1	Cu ₂	1	Sb ₄	1
As ₃	1	CuO	1	SbH ₃	1
As ₄	1	CuS	1	SbCl ₃	1
As(OH) ₃	1	CuCl	1	SbCl ₅	1
AsH ₃	1	Cu ₃ Cl ₃	1	SbS	1
AsCl ₃	1	H ₂	5	Se	1
AsS	1	H ₂ O	5	Se ₂	1
As ₂ O ₆	1	HCl	5	Se ₃ O	1
Au	1	HClO	1	Se ₄	1
AuCl(H ₂ O)	3	HS	1	Se ₅	1
AuCl(H ₂ O) ₂	3	H ₂ S	5	Se ₆	1
AuCl(H ₂ O) ₃	3	H ₂ Se	6	Se ₇	1
AuCl(H ₂ O) ₄	3	H ₂ SO ₄	1	Se ₈	1
AuS	4	Hg	1	SeO	1
AuS(H ₂ O)	4	HgO	1	SeO ₂	1
AuS(H ₂ O) ₂	4	HgH	1	SeCl ₂	1
AuS(H ₂ O) ₃	4	HgCl ₂	1	Se ₂ Cl ₂	1
AuS(H ₂ S)	4	HgS	1	SeS	1
AuS(H ₂ S)(H ₂ O)	4	HgSe	1		
AuS(H ₂ S)(H ₂ O) ₂	4	O ₂	5		
AuS(H ₂ S)(H ₂ O) ₃	4	S	1		
AuS(H ₂ S)(H ₂ O) ₄	4	S ₂	5		

References: 1 – Yokokawa (1988); 2 – Akinfiev and Zotov (2016); 3 – Hurtig and Williams-Jones (2014); 4 – Hurtig and Williams-Jones (2015); 5 – Reid et al. (1977); 6 – Akinfiev and Tagirov (2006).

calculated from two-parameter and three-parameter equation of state by Breedveld and Prausnitz (1973) and by Lee and Kesler (1975), respectively.

3. Geologic setting of the Rogovik Au-Ag deposit

3.1. Regional geology

The Okhotsk-Chukchi volcanic belt (OCVB) is the longest segment of East Asian volcanoplutonic belts (Fig. 1a). The Balygychan-Sugoi trough is one of the main metalliferous structures of the OCVB (Kuznetsov and Livach, 2005; Sidorov et al., 2009). The trough extends in east-west direction for > 250 km, ranging from 15 to 40 km in width. It is related to the deep Balygychan fault.

The Balygychan-Sugoi trough is bounded by the Dogdo-Eriket mercury belt located in the northern part of the OCVB (Gamyani et al., 2003; Shpikerman and Goryachev, 1996). The Dogdo-Eriket metallogenic belt hosts gold-silver, silver-polymetallic and mercury zones (Kostin and Denisov, 2007; Kostin et al., 2011; Krylova and Kichigin, 1989).

The area of the Balygychan-Sugoi trough is underlain by the Verkhojansk complex, which consists of Permian to Jurassic marine clastic units and is unconformably overlain and/or intruded by a complex unit of the Early Cretaceous igneous rocks, which are related to the first stage of trough formation and include potassic rhyolites and rhyodacites (Askol'd formation) (Konstantinov et al., 1998). The Early Cretaceous volcanic rocks are in turn overlain by the Early Cretaceous coaliferous molasse (Omsukchan formation). The Early to Late Cretaceous effusives of the Tavatum formation consist of andesites and andesitic tuffs. These rocks are overlain by Late Cretaceous rhyolites, ignimbrites and rhyolite tuffs of the Nayakhan formation, which are

Table 3

Minerals of system Na–K–Mg–Ca–Al–Si–Ti–Mn–Fe–Cu–Zn–Pb–Ag–Au–Hg–As–Sb–S–Se–Cl–C–H–O and solid solutions used in the calculations.

Mineral	Formula	Ref	Mineral	Formula	Ref
Ag–Au–Hg	Au _x Ag _y Hg _{1-x-y}	1	Metacinnabar	HgS	6
Ag ₂ S–Ag ₂ Se	Ag ₂ S _x Se _{1-x}	2	Goethite	FeO(OH)	5
Petrovskaitite	AgAuS	3	Iron Oxide	FeO	6
Uytenbogaardtite	Ag ₃ AuS ₂	3	Hematite	Fe ₂ O ₃	9
Chlorargyrite	AgCl	4	Magnetite	Fe ₃ O ₄	9
Silver Oxide	Ag ₂ O	5	Westerveldite	FeAs	15
Böhmite	AlO(OH)	6	Löllingite	FeAs ₂	15
Diaspore	AlO(OH)	6	Arsenopyrite	FeAsS	15
Gibbsite	Al(OH) ₃	6	Scorodite	FeAsO ₄ (H ₂ O) ₂	16
Dickite	Al ₂ Si ₂ O ₅ (OH) ₄	7	Pyrrhotite	FeS	6
Kaolinite	Al ₂ Si ₂ O ₅ (OH) ₄	6	Pyrite	FeS ₂	6
Arsenic	As	8	Gudmundite	FeSbS	17
Arsenolite	As ₂ O ₃	8	Berthierite	FeSb ₂ S ₄	17
Claudette	As ₂ O ₃	8	Seinajokite	FeSb ₂	17
Realgar	AsS	8	Ferrosilite	FeSiO ₃	6
Orpiment	As ₂ S ₃	8	Sylvite	KCl	6
Graphite	C	9	Alunite	KAl ₃ (SO ₄) ₂ (OH) ₆	6
Titanite	CaTiSiO ₅	9	Phlogopite	KMg ₃ AlSi ₃ O ₁₀ (OH) ₂	6
Gehlenite	Ca ₂ Al ₂ SiO ₇	9	Annite	KFe ₃ AlSi ₃ O ₁₀ (OH) ₂	6
Grossular	Ca ₃ Al ₂ Si ₃ O ₁₂	6	KFsp	KAlSi ₃ O ₈	9
Andradite	Ca ₃ Fe ₂ Si ₃ O ₁₂	6		NaAlSi ₃ O ₈	9
Diopside	CaMg(SiO ₃) ₂	6	Muscovite	KAl ₃ Si ₃ O ₁₀ (OH) ₂	9
Hedenbergite	CaFe(SiO ₃) ₂	6		NaAl ₃ Si ₃ O ₁₀ (OH) ₂	9
Akermanite	Ca ₂ MgSi ₂ O ₇	6	Halite	NaCl	6
Wairakite	CaAl ₂ Si ₄ O ₁₂ (H ₂ O) ₂	10	Mopungite	NaSb(OH) ₆	18
Margarite	CaAl ₄ Si ₂ O ₁₀ (OH) ₂	10	Dawsonite	NaAlCO ₃ (OH) ₂	7
Prehnite	Ca ₂ Al ₂ Si ₃ O ₁₀ (OH) ₂	9	Analcime	NaAlSi ₂ O ₆ H ₂ O	6
Tremolite	Ca ₂ Mg ₅ Si ₈ O ₂₂ (OH) ₂	11	Paragonite	NaAl ₂ AlSi ₃ O ₁₀ (OH) ₂	6
Anhydrite	CaSO ₄	6	Plagioclase	NaAlSi ₃ O ₈	9
Gypsum	CaSO ₄ (H ₂ O) ₂	5		CaAl ₂ Si ₂ O ₈	9
Carbonates	CaCO ₃	9	Pargasite	NaCa ₂ Mg ₄ AlAl ₂	
	MgCO ₃	9		Si ₆ O ₂₂ (OH) ₂	6
	MnCO ₃	9	Ferropargasite	NaCa ₂ Fe ₄ AlAl ₂	6
	FeCO ₃	9		Si ₆ O ₂₂ (OH) ₂	
Dolomite	CaMg(CO ₃) ₂	9	Periclase	MgO	6
Huntite	CaMg ₃ (CO ₃) ₄	10	Brookite	Mg(OH) ₂	6
Copper	Cu ⁰	10	Enstatite	MgSiO ₃	6
Tenorite	CuO	10	Sepiolite	Mg ₄ Si ₆ O ₁₅ (OH) ₂ (H ₂ O) ₂ (H ₂ O) ₄	6
Cuprite	Cu ₂ O	10	Artinite	Mg ₂ CO ₃ (OH) ₂ (H ₂ O) ₃	6
Covellite	CuS	10	Chrysolite	Mg ₃ Si ₂ O ₅ (OH) ₄	6
Chalcocite	Cu ₂ S	10	Talc	Mg ₃ Si ₄ O ₁₀ (OH) ₂	9
Cuprostibite	Cu ₂ Sb	12	Anthophyllite	Mg ₇ Si ₈ O ₂₂ (OH) ₂	6
Domeykite	Cu ₃ As	12	Antigorite	Mg ₄₈ Si ₃₄ O ₈₅ (OH) ₆₂	6
Azurite	Cu ₃ (CO ₃) ₂ (OH) ₂	6	Chlorite	Mg ₆ Si ₄ O ₁₀ (OH) ₈	9
Malachite	Cu ₂ (CO ₃)(OH) ₂	6		Mg ₄ Al ₄ Si ₂ O ₁₀ (OH) ₈	9
Chalcopyrite	CuFeS ₂	6		Mg ₅ Al ₂ Si ₃ O ₁₀ (OH) ₈	9
Bornite	Cu ₅ FeS ₄	6		Fe ₅ Al ₂ Si ₃ O ₁₀ (OH) ₈	9
Tetrahedrite	Cu ₁₀ Fe ₂ Sb ₄ S ₁₃	13	Litharge	PbO	19
Montroydite	HgO	14	Galena	PbS	6
Cinnabar	HgS	6	Anglesite	PbSO ₄	6
Cerussite	PbCO ₃	6	Quartz	SiO ₂	9
Native sulfur	S	19	Rutile	TiO ₂	9
Native stibium	Sb	14	Zinc	Zn	12
Senarmontite	Sb ₂ O ₃	20	Zinc arsenide	Zn ₃ As ₂	12
Valentinite	Sb ₂ O ₃	20	Zincite	ZnO	19
Cervantite	Sb ₂ O ₄	14	Wurtzite	ZnS	6
Stibnite	Sb ₂ S ₃	20	Sphalerite	ZnS	6

References: 1 – Chudnenko and Pal'yanova (2013); 2 – Pal'yanova et al. (2014); 3 – Tagirov et al. (2006); 4 – Akiniev and Zotov (2016); 5 – Naumov et al. (1974); 6 – Helgeson et al. (1978); 7 – Robie and Hemingway (1995); 8 – Pokrovski et al. (1996); 9 – Holland and Powell (1998); 10 – Johnson et al. (1992); 11 – Berman (1988); 12 – Yokokawa (1988); 13 – Seal et al. (1990); 14 – Bessinger and Apps (2003); 15 – Perfetti et al. (2008); 16 – Fujita et al. (2009); 17 – Williams-Jones and Normand (1997); 18 – Diemar (2008); 19 – Shock et al. (1997); 20 – Zotov et al. (2003).

related to the final volcanoplutonic stage of trough formation. In the Paleogene, dikes and a thin basalt cover were formed.

The Nyagain volcanic structure occurs at the northern end of the Balygchan-Sugoi trough. The central part of this structure is composed of rhyolite lavas forming the volcanic dome with volcanic-sedimentary rocks on the periphery. In the northwestern peripheral part of this structure is the Au–Ag Rogovik deposit (Kuznetsov et al., 1992).

The Au–Ag Rogovik deposit (Kravtsova et al., 2015; Kuznetsov et al., 1992) is either related to the cryptovolcanic edifice of the Nyagain

volcanic structure or to the thick extended fault zone, cross cutting the Balygchan-Sugoi trough in east-west direction. The Dolinnyi fault zone controls the Late Cretaceous–Paleogene Dogdo-Erikrit mercury belt (Gamyaniin et al., 2003; Shpikerman and Goryachev, 1996), which bounds the southeastern flank of the Rogovik deposit, enriched in mercury. Stratigraphic and structural data suggest a Late Cretaceous age for early stage Au–Ag mineralization (Kuznetsov et al., 1992) in the absence of radiometric dating. The Rogovik deposit is in the prospecting stage.

Table 4
Paragenetic sequence of ore and gangue minerals in different types of ore mineral assemblages from the Rogovik deposit.

Minerals	Stages		
	I – volcanic Au-Ag	II – volcanoplutonic Ag-Pb Ag-Au-Pb	
Gangue minerals			
Quartz	—————	—————	—————
Adularia	—————	—————	—————
Sericite	—————	—————	—————
Illite	—————	-----	-----
Jarosite	—————	-----	-----
Kaolinite	-----	-----	-----
Orthoclase	-----	—————	—————
Chlorite	-----	-----	-----
Albite	-----	-----	-----
Carbonates	-----	-----	-----
Carbonaceous-substance	-----	-----	-----
Ore minerals			
Pyrite	—————	—————	—————
Electrum	—————	—————	—————
Kustelite	—————	—————	—————
High-finesness gold	—————	—————	-----
Acanthite	—————	-----	-----
Proustite	-----	-----	-----
Pyrargyrite	-----	-----	-----
Stephanite	-----	-----	-----
Native silver	-----	-----	-----
Silver amalgams	-----	-----	-----
Gold-silver amalgams	-----	-----	-----
Tetrahedrite	-----	-----	-----
Freibergite	-----	-----	-----
Naumannite	-----	-----	-----
Argyrodite	-----	-----	-----
As-polybasite	-----	-----	-----
Chalcostibite	-----	-----	-----
Hessite	-----	-----	-----
Canfieldite	-----	-----	-----
Imiterite	-----	-----	-----
Galena	-----	-----	-----
Sphalerite	-----	-----	-----
Chalcopyrite	-----	-----	-----
Arsenopyrite	-----	-----	-----

Note: The line thickness marks the relative mineral abundance, and the dashed line shows that the mineral of sporadic occurrence.

3.2. Deposit geology

The Rogovik Au-Ag deposit is hosted by the Lower Cretaceous volcano-sedimentary rocks of the Omsukchan formation. These rocks comprise siltstones with bands of carbon-bearing slates, volcanoclastic sandstones, ignimbrites, rhyolitic tuffs and tuffaceous breccia (Fig. 1c). Mineralized zones are hosted mainly by ash and vitroclastic tuffs of rhyolite composition and tuffaceous breccia. Hydrothermal alteration related to the early volcanic stage includes argillic alteration and silicification. They dominate in the upper levels. These alteration assemblages consist of quartz, adularia, sericite, illite, clay minerals (jarosite, kaolinite), and pyrite (Table 4). Interstices between the quartz and adularia grains are filled with iron hydroxides and graphite particles. At the middle and lower levels of the deposit, alteration assemblages are related to the late volcanoplutonic stage and consist of quartz-(orthoclase)-adularia-sericite and quartz-(adularia)-orthoclase-sericite-carbonate (Table 4). With depth, carbonates replace clay minerals and adularia, the amount of sericite increases and chlorite appears. In the deepest parts of the mineralized zone, hydrothermal alteration is characterized by the assemblages of quartz-orthoclase-carbonate and quartz-carbonate-sericite-chlorite.

The ore bodies have no clear boundaries and differ, mainly, in concentrations of Au and Ag. At the upper levels, the ore bodies are represented by the zones of veinlet mineralization and at the deeper levels, by veinlet and disseminated mineralization. The morphology of ore bodies is linear to areal. The dip of mineralized zones varies from gentle to steep with depth. The width of zones ranges from 10 m to 160 m and more. The thickness of veins and veinlets varies from few mm to 4–8 cm and, in places, to 10–20 cm. The explored length of ore

zones is 2000 m along the strike and about 400 m down dip (Kravtsova et al., 2015).

3.3. Mineralization

The paragenetic sequence of ore minerals (Table 4) is divided into two main stages, namely the early volcanic and the late volcanoplutonic stage (Kravtsova et al., 2012, 2015). Formation of Au-Ag mineral assemblages, which exhibit typical characteristics of the epithermal low-sulfidation type, is related to the early volcanic stage. Ag-Pb and Ag-Au-Pb mineral assemblages were formed at the late volcanoplutonic stage spatially overlapping with Au-Ag mineralized zones of the early volcanic stage.

3.3.1. Early volcanic stage

The Au-Ag mineralized zones occur in the central part of the deposit, mostly at the upper levels of the ore body. Ore minerals occur in banded and colloform adularia-quartz veins and veinlets. The ore samples contain Au (< 6.04 ppm), Ag (< 40 ppm), As (< 800 ppm), Sb (< 50 ppm), Se (< 15.8 ppm) and Hg (< 2.7 ppm). The content of S is low (< 1 wt%), consistent with the formation model of the low-sulfidation epithermal type.

The main ore minerals are pyrite, electrum, kustelite and Ag-bearing minerals, with minor galena, sphalerite, and chalcopyrite (Table 4). The gold-acanthite-naumannite assemblage hosted by adularia-quartz veins is the highest in grade. The Ag-bearing minerals, such as acanthite (Ag₂S), silver sulfosalts (proustite, Ag₃AsS₃; pyrargyrite, Ag₃SbS₃) and naumannite (Ag₂Se), are abundant, whereas stephanite and native silver are rare. Acanthite occurs as inclusions in pyrite and quartz and is intergrown with electrum and silver sulfosalts in adularia-quartz aggregates (Fig. 2a) Acanthite forms intergrowths with S-naumannite, but unlike the latter it is cataclazed, which suggests the earlier deposition of silver sulfide during ore-formation. Silver sulfoselenides of the naumannite series contain S impurities ranging from 0.12 to 3.52 wt% (Table 5), which corresponds to the range of compositions from Ag_{2.8}S_{0.36}Se_{0.64} to Ag_{2.19}S_{0.01}Se_{0.99} (Fig. 3a). Acanthite (Ag₂S–Ag_{2.3}S_{0.87}Se_{0.13}) contains Fe (0–7.46 wt%), Se (0–3.21 wt%), as well as Hg (< 3.24 wt%) and Au (< 0.74 wt%) (Table 5). Compositions of pyrargyrite show impurities of < 0.16 wt% Se and < 0.12 wt% Au and compositions of stephanite show impurities of < 1.42 wt% Se, < 0.12 wt% Au and 0.16–0.20 wt% Hg (Table 5).

Electrum commonly occurs as isometric grains and may occasionally exhibit irregular shapes. The grain size ranges from fine-dispersed (1–10 μm) to small (10–70 μm) with large grains (70–130 μm) being very rare. Electrum is intergrown with acanthite and silver sulfosalts in quartz-adularia aggregates and occurs as inclusions in naumannite and pyrite (Fig. 2b). Anhedral grains of kustelite occur as inclusions in quartz. Compositions of electrum and kustelite are shown in Fig. 3b and Table 5. Mercury is constantly present, with the highest content being 15.9 wt% in kustelite and 2 wt% in electrum.

3.3.2. Late volcanoplutonic stage

The Ag-Pb mineral assemblages are hosted by sericite-quartz, sericite-orthoclase-quartz and quartz veinlets. The main gangue mineral is quartz and less frequently adularia, which shows replacement textures after orthoclase and sericite. Ag-Pb mineralized zones are confined mainly to the intermediate depth intervals. These zones are of north-eastern strike and intersect Au-Ag mineralized zones. The ore samples show extremely low Au (> 0.2 ppm) and concentrations of > 1000 ppm Ag. Further, these samples contain high concentrations of Hg (< 46.5 ppm), Se (< 132.8 ppm), As (< 600 ppm), Sb (< 200 ppm) and B (300 ppm), with elevated Cu (< 300 ppm), Pb (< 600 ppm) and Zn (< 500 ppm). The concentration of S ranges up to 15.4 wt%, which is not consistent with the Au-Ag low-sulfidation epithermal type.

The main ore minerals are pyrite, galena, sphalerite, native silver, tetrahedrite, silver sulfoselenides and sulfosalts, with minor

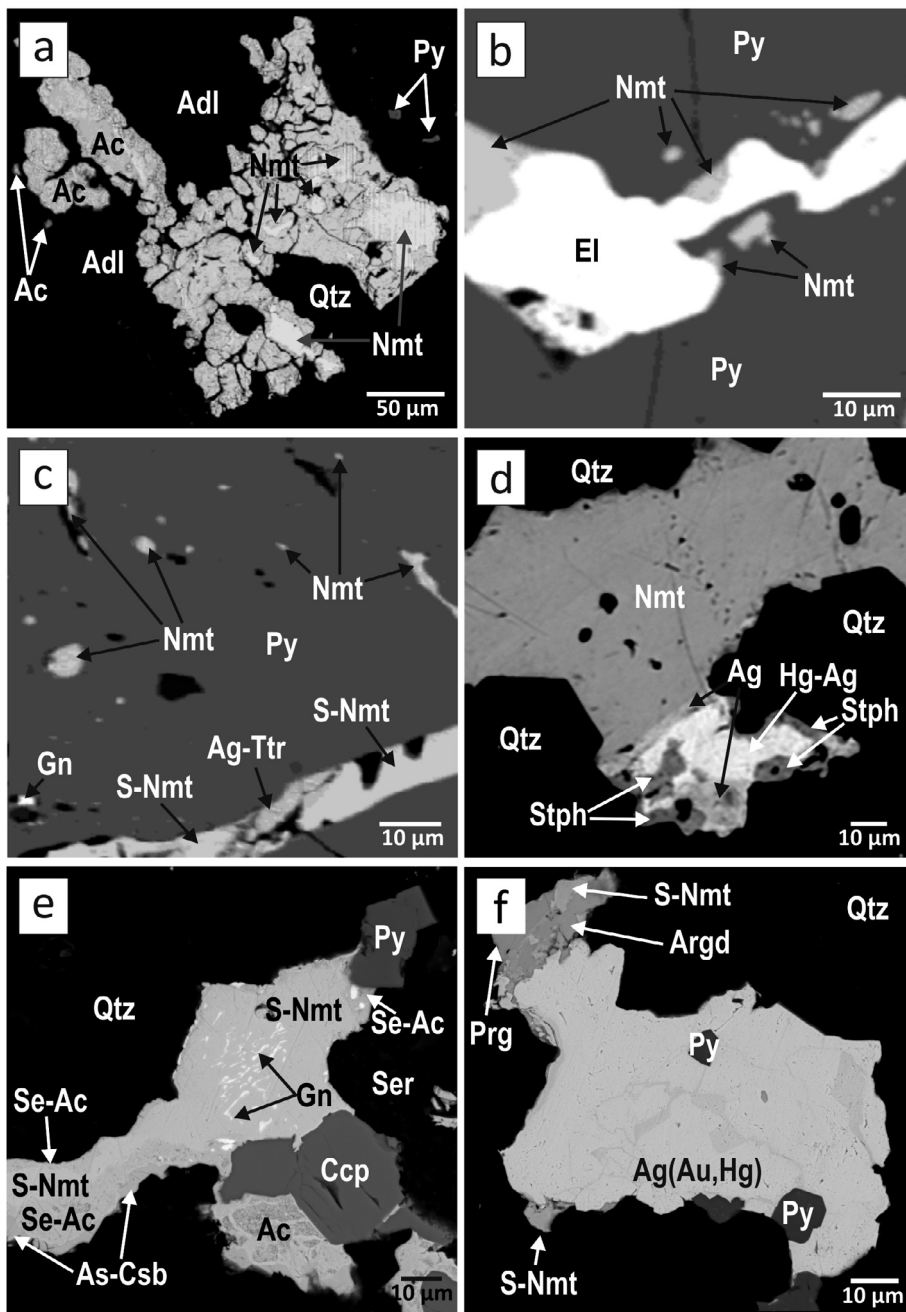


Fig. 2. SEM photomicrographs of Au- and Ag-bearing minerals in Au-Ag (a and b), Ag-Pb (c and d) and Ag-Au-Pb (e and f) types of mineral assemblages. (a) Cataclazed acanthite (Ac) replaced by naumannite (Nmt) in quartz-adularia (Qtz-Adl) aggregate; (b) Intergrown electrum (El) and naumannite (Nmt) inclusions in pyrite (Py); (c) Microinclusions of naumannite (Nmt) and galena (Gn) in pyrite and later naumannite-tetrahedrite veinlet cross cutting pyrite; (d) Naumannite (Nmt) intergrown with native silver (Ag) and silver amalgams (Hg-Ag) replaced by stephanite (Stph); (e) S-naumannite (S-Nmt) containing exsolution lamellae of galena (Gn) intergrown with chalcocopyrite (Ccp), acanthite (Ac) and pyrite (Py) and surrounded by a border of Se-acanthite (Se-Ac) and As-chalcostibite (As-Csb) in quartz-sericite (Qtz-Ser) aggregate; (f) Hg-rich kustelite and electrum (Ag (Au, Hg)) intergrown with pyrite (Py), S-naumannite (S-Nmt), argyrodite (Argd) and pyrargyrite (Prg) in quartz aggregate.

chalcocopyrite (Table 4). The native silver – sulfosalts mineral assemblage hosted by sericite-quartz veinlets is the highest in grade.

Naumannite occurs as inclusions in pyrite and in association with native silver and stephanite forming veinlets cross cutting pyrite (Fig. 2c). Silver selenide constantly contains S in amounts from 0.42 to 3.52 wt% corresponding to $Ag_{1.85}Se_{0.71}S_{0.29}$ – $Ag_{2.6}Se_{0.95}S_{0.05}$. In addition, Hg reaches 0.2 wt% (Table 6). Acanthite ($Ag_{1.47}S_{0.094}Se_{0.06}$ – $Ag_{1.44}S_{0.85}Se_{0.15}$) contains Fe (0–0.95 wt%) and Se (2.36–6.06 wt%) as impurities (Table 6). Compositions of pyrargyrite, stephanite and polybasite were also analyzed showing high amounts of Se (< 2.60 wt%) in polybasite.

Native silver occurs as irregularly shaped grains with sizes up to 30 μm . It is intergrown with silver sulfosalts and naumannite and also occurs as disseminated inclusions in quartz (Fig. 2d). Native silver shows high Hg (< 18.95 wt%) and is also referred to as silver amalgams (Fig. 3b). Silver amalgams also contain impurities of S (0.15–1.8 wt%), Se (< 1.1 wt%), Sb (< 3.4 wt%) and Cu (< 1.8 wt%)

(Table 6). The high Ag and Hg contents are distinctive features of this mineral assemblage.

The Ag-Au-Pb mineral assemblage occurs increasingly with depth and has more complex composition than Ag-Pb assemblages found at moderate depth. Mineralized zones are characterized by veined and veined-disseminated mineralization in pervasively altered rocks. The main ore forming components are Ag and Au, which are hosted in quartz-albite-(orthoclase)-carbonate veins. These ores display the highest of Ag (< 10000 ppm) and Au (< 260 ppm). The Ag-Au-Pb samples show Zn (< 2000 ppm), Pb (< 1000 ppm), Cu (< 1000 ppm), Se (< 685 ppm), Sb (< 600 ppm), As (< 500 ppm), Hg (< 168 ppm), Ge (> 100 ppm), Te (< 27 ppm), Bi (< 15 ppm) and S (< 18.32 wt%), indicating a more complex mineralogy compared to the other two mineral assemblages found at the Rogovik deposit. The main ore minerals are pyrite, galena, sphalerite, chalcocopyrite, electrum, kustelite, native silver, tetrahedrite, argyrodite, silver sulfoselenides and sulfosalts, with minor hessite, chalcostibite, canfieldite, imiterite and arsenopyrite (Table 4).

Table 5
Representative EPMA analyses of major ore minerals from Au-Ag ore mineral assemblages from the Rogovik deposit (in wt%, – below detection limit).

Au	Ag	Hg	Sb	As	Cu	Se	Fe	S	Σ
Electrum and Hg-rich electrum									
69.44	30.54	< 0.15	–	–	–	–	< 0.05	–	100.18
40.98	56.29	1.89	–	–	–	–	–	–	99.16
70.41	27.87	1.61	–	–	–	–	–	–	99.89
39.41	58.02	1.63	–	–	–	–	–	–	99.06
70.52	29.44	–	–	–	–	–	–	–	99.96
Hg-rich kustelite									
20.38	76.38	0.30	–	–	–	–	0.98	1.07	99.11
16.98	65.29	15.89	–	–	–	–	–	–	98.16
24.62	73.63	0.62	–	–	–	–	< 0.05	< 0.15	99.06
Hg-rich silver									
< 0.12	99.92	< 0.15	< 0.14	–	–	< 0.16	–	< 0.15	100.64
0.89	96.87	1.70	0.51	–	–	< 0.16	–	0.58	100.71
1.86	95.08	1.50	0.41	–	–	< 0.16	–	1.21	100.22
Acanthite									
–	86.75	–	–	–	< 0.10	1.42	–	11.79	100.06
0.74	77.54	3.24	–	–	–	3.21	5.58	9.01	99.32
–	83.28	–	–	–	0.63	–	< 0.05	14.61	98.57
0.16	78.39	1.28	–	–	–	0.73	3.56	15.76	99.88
0.58	78.13	1.05	–	–	–	2.73	7.46	8.27	98.22
S-naumannite									
–	77.94	–	–	–	–	16.05	2.40	3.52	99.91
–	82.35	–	–	–	–	13.45	0.89	3.10	99.79
–	75.05	–	–	–	–	24.85	–	0.12	100.02
Pyrargyrite									
< 0.12	60.04	–	22.88	–	–	< 0.16	–	17.07	100.27
–	59.00	–	22.77	–	–	–	–	18.19	99.96
–	61.20	–	21.28	–	–	–	–	17.55	100.03
Stephanite									
< 0.12	70.10	0.16	15.23	–	–	0.70	–	14.05	100.36
–	68.01	0.18	14.85	–	–	1.42	–	15.89	100.35
–	68.65	< 0.20	15.25	–	–	0.42	–	16.09	100.61
Pyrite									
< 0.12	–	–	–	1.85	–	–	44.37	53.75	100.09
0.22	< 0.12	–	< 0.14	0.38	–	< 0.16	45.52	53.90	100.44

S-naumannite is present as inclusions in pyrite and argyrodite and forms intergrowths with the latter. This mineral is in close association with galena, sphalerite and chalcopyrite and fills cracks in fractured pyrite crystals (Fig. 2e). Se-acanthite occurs as small inclusions in quartz and forms replacement rims on silver sulfoselenides of the naumannite series, pyrite, chalcopyrite and silver sulfosalts or fills

cracks and veinlets in pyrite, sphalerite and chalcopyrite. Fig. 3a shows composition of silver sulfoselenides of the acanthite and naumannite series, respectively, for the Ag-Au-Pb mineral assemblage. Generalized intervals of the acanthite and naumannite series correspond to the range of compositions from Ag_2S to $Ag_2S_{0.74}Se_{0.26}$ and from $Ag_2S_{0.28}Se_{0.72}$ to Ag_2Se , respectively. Au and Hg were found in

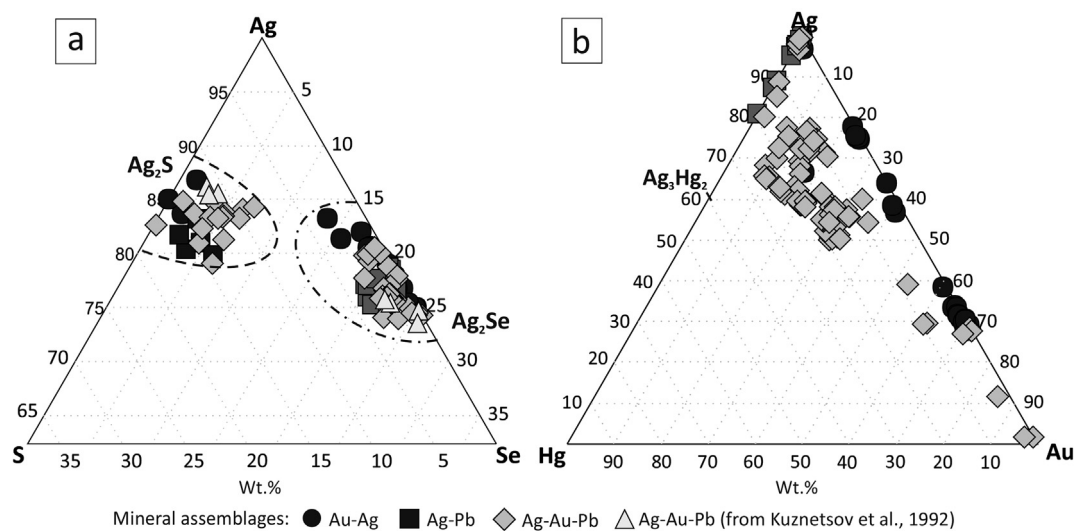


Fig. 3. Variations in compositions of (a) silver sulfoselenides and (b) Au-Ag-Hg solid solutions (wt%) in mineral assemblages from the Rogovik deposit (according to the literature and our own data).

Table 6

Representative EPMA analyses of major ore minerals from Ag-Pb ore mineral assemblages from the Rogovik deposit (in wt%, – below detection limit).

Ag	Hg	Sb	As	Cu	Pb	Zn	Se	Te	Fe	S	Σ
Hg-rich silver											
99.85	< 0.15	< 0.14	–	–	–	–	< 0.16	–	–	< 0.15	99.85
84.93	4.14	3.39	–	1.84	–	0.55	1.11	1.29	1.14	1.77	100.16
81.09	18.95	< 0.14	–	< 0.10	–	< 0.10	< 0.16	< 0.20	< 0.05	< 0.15	100.04
82.92	10.21	1.28	–	0.95	–	0.57	1.05	1.30	1.09	0.70	100.07
Se-acanthite											
75.70	–	–	–	1.46	–	–	4.42	–	0.95	16.22	98.75
80.24	–	–	–	–	–	–	6.06	–	–	14.10	100.40
81.08	–	–	–	0.63	–	–	2.36	–	–	15.61	99.68
S-naumannite											
74.71	–	–	–	–	–	–	22.51	–	0.70	2.53	100.45
78.57	0.20	–	–	–	–	–	20.98	–	–	0.42	100.16
74.94	–	–	–	–	–	–	21.05	–	0.40	3.52	99.91
Pyrrargyrite											
60.04	–	20.62	1.00	< 0.10	–	–	1.20	–	< 0.05	17.07	99.93
61.02	–	19.04	1.10	–	–	–	1.02	–	–	18.14	100.32
Stephanite											
68.65	< 0.15	15.25	–	–	–	–	0.42	–	–	16.09	100.41
68.53	–	14.88	–	0.16	–	–	1.87	–	–	14.51	99.95
Polybasite											
62.77	–	10.85	–	8.97	–	–	1.83	–	–	16.25	100.66
67.51	–	9.14	–	5.53	–	–	2.60	–	–	15.22	100.00
Tetrahedrite											
< 0.12	–	25.54	–	49.78	–	–	< 0.16	–	0.62	24.01	99.95
0.58	–	26.14	–	50.11	–	–	–	–	< 0.05	23.24	100.07
Freibergite											
22.88	< 0.15	29.48	–	24.75	–	–	< 0.16	–	< 0.05	22.94	100.05
28.54	0.21	22.70	–	20.71	–	–	1.93	–	5.13	20.91	100.13
Pyrite											
< 0.12	< 0.15	< 0.14	–	< 0.10	–	–	0.46	–	46.39	53.13	99.98
5.46	–	–	–	–	–	–	1.03	–	44.31	50.66	100.45
Chalcopyrite											
< 0.12	–	–	–	35.28	–	–	0.50	–	29.77	34.37	99.92
–	–	–	–	35.03	–	–	0.15	–	29.92	35.03	100.13
Galena											
0.33	–	–	–	–	84.71	–	0.44	–	–	13.72	99.17
0.45	–	–	–	< 0.10	86.25	–	< 0.16	–	< 0.05	12.89	99.59
Sphalerite											
< 0.12	–	–	–	–	< 0.15	65.98	< 0.16	–	1.39	33.22	100.59
–	–	–	–	–	–	65.26	–	–	1.54	32.91	99.96

polybasite (< 0.65 and < 0.15 wt%, respectively) and hessite (< 4.40 and < 0.15 wt%), whereas stephanite, pyrrargyrite and freibergite contain only minor amounts of Hg (~0.21 wt%). Elevated Se impurities were found in polybasite (< 4.60 wt%) (Table 7).

Hg-rich kustelite and electrum (Fig. 3b) with grain sizes from 10 to 320 μm occur in close associations with the Ag-bearing minerals. The detected admixtures are Fe to 1.1 wt% and Hg to 9.4 wt%, less common are Cu to 0.41 wt% and Zn to 0.11 wt%. Kustelite (lighter grains) (Fig. 2f) contains Ag < 70.34 wt% and Hg < 21.22 wt%, and kustelite (dark veinlets) corresponds to the compositions with Ag < 81.24 wt% and Hg < 10.5 wt% (Table 7). Electrum is characterized by wide variations of silver, gold and mercury and different compositions of trace elements (Table 7).

Silver amalgams are associated with acanthite, silver sulfosalts (mainly stephanite), naumannite and argyrodite and frequently replace those minerals and/or form rims around them. Silver amalgam inclusions with sizes of > 50 μm also were found in Hg-rich kustelite and electrum and their composition is shown in Table 7.

4. Fluid inclusions

4.1. Petrography of fluid inclusions

Fluid inclusions (FI) that were found as isolated FIs and FI assemblages are of round vacuole shape and occur in the growth zones of quartz grains, which were interpreted as primary in origin, and those aligned along micro-fractures in cross-cutting trails, which were interpreted as pseudosecondary and secondary in origin (Roedder, 1984).

The studied quartz grains from adularia-quartz aggregates formed at the early ore-forming stage contain disseminated Au-Ag mineralization (pyrite + electrum ± galena), which suggests the simultaneous formation of gangue and ore minerals, and healed veinlets of Au-Ag mineralization (pyrite + electrum + silver sulfosalts). Therefore, we focused our study on the primary and pseudosecondary fluid inclusions, respectively. Three fluid inclusions types were identified at room temperature in these adularia-quartz aggregates: aqueous liquid-rich inclusions (Lw) (Fig. 4a and b), aqueous vapor-rich inclusions (Vw)

Table 7

Representative EPMA analyses of major ore minerals from Ag-Au-Pb ore mineral assemblages from the Rogovik Au-Ag deposit (in wt%, – below detection limit).

Au	Ag	Hg	Sb	As	Cu	Pb	Zn	Se	Te	Fe	S	Ge	Bi	Σ	
Hg-rich silver															
1.12	96.50	2.20	0.24	–	–	–	< 0.10	–	< 0.20	–	< 0.15	–	–	100.06	
0.62	88.62	10.50	0.16	–	–	–	< 0.10	–	–	< 0.05	< 0.15	–	–	99.90	
9.12	64.73	24.61	–	–	–	–	–	–	–	–	–	–	–	98.46	
Hg-rich kustelite															
13.02	77.7	9.69	–	–	–	–	–	–	–	< 0.05	–	–	–	100.41	
19.85	69.30	9.19	–	–	–	–	–	–	–	1.62	–	–	–	99.96	
15.59	70.34	12.61	–	–	–	–	–	–	–	0.45	0.25	–	–	99.25	
19.11	59.76	18.03	2.23	–	–	–	–	0.34	–	–	–	–	–	99.46	
Hg-rich electrum															
31.80	55.47	11.92	–	–	0.09	–	–	0.37	–	< 0.05	< 0.15	–	–	99.68	
30.90	50.44	19.24	–	–	–	–	–	–	–	0.63	–	–	–	101.21	
71.61	27.67	< 0.15	–	–	–	–	–	–	–	1.09	–	–	–	100.37	
60.66	29.39	9.43	–	–	0.41	–	–	–	–	–	–	–	–	99.89	
Hg-rich high-fineness gold															
85.35	11.61	2.58	< 0.14	–	–	–	–	–	–	–	–	–	–	99.54	
98.15	1.84	< 0.15	–	–	–	–	–	–	–	–	–	–	–	99.99	
Se-acanthite															
–	82.41	–	–	–	–	–	–	7.45	–	–	9.11	–	–	98.97	
0.74	77.54	3.24	–	–	–	–	–	3.21	–	4.31	11.01	–	–	100.05	
–	80.71	–	–	–	–	–	–	< 0.16	0.79	–	16.81	0.36	–	98.67	
S-naumannite															
< 0.12	62.89	–	–	–	0.66	–	–	34.61	–	< 0.05	0.35	–	–	98.51	
–	77.05	–	–	–	–	–	–	19.19	–	–	2.90	–	–	99.14	
Stephanite															
–	68.35	0.12	15.25	–	–	–	–	0.42	–	–	16.09	–	–	100.12	
–	68.29	–	12.89	–	1.53	–	–	2.1	–	–	15.23	–	–	100.04	
Pyrargyrite															
–	60.70	0.18	21.15	1.05	–	–	–	< 0.16	–	–	17.06	–	–	100.15	
–	61.90	0.16	22.05	1.03	–	–	–	–	–	–	15.06	–	–	100.21	
Polybasite															
0.65	70.581	< 0.15	9.41	< 0.10	2.38	–	–	4.00	–	–	12.98	–	–	100.00	
0.59	60.81	–	11.25	< 0.10	5.31	–	0.58	4.59	4.77	0.32	11.91	–	–	100.12	
Tetrahedrite															
< 0.12	1.32	–	24.47	–	47.18	–	1.10	< 0.16	< 0.20	0.52	24.01	–	1.50	100.10	
–	0.40	–	25.02	–	48.11	–	1.30	–	–	1.02	23.24	–	1.28	100.37	
Freibergite															
–	26.57	–	21.20	–	28.87	–	0.59	< 0.16	–	0.76	22.55	–	–	100.54	
–	30.54	0.21	22.76	–	23.71	–	–	1.93	–	0.13	20.91	–	–	100.19	
Hessite															
4.40	60.51	–	–	–	–	–	–	–	36.58	< 0.05	< 0.15	–	–	100.18	
< 0.12	60.11	–	0.71	–	1.02	–	–	1.30	35.16	1.01	0.89	–	–	100.19	
Argyrodite															
< 0.12	75.10	–	–	–	–	–	–	1.25	< 0.20	–	17.03	6.53	–	99.91	
–	76.17	–	0.30	–	–	–	–	4.33	–	0.30	14.40	5.38	–	100.88	
Pyrite															
2.32	2.31	2.70	–	–	–	–	–	0.56	–	44.37	49.64	–	–	99.91	
Galena															
–	1.67	–	–	–	–	81.45	–	2.52	–	< 0.05	12.32	–	–	100	
–	0.36	–	–	–	< 0.10	85.81	–	1.42	–	< 0.05	12.02	–	–	99.61	
Sphalerite															
< 0.12	2.33	–	–	–	–	–	61.30	–	1.37	2.77	32.15	–	–	99.92	
0.80	< 0.12	–	–	–	–	< 0.10	61.45	< 0.16	–	3.29	34.88	–	–	100.39	
Arsenopyrite															
< 0.12	–	–	–	46.56	–	–	< 0.10	–	–	30.75	22.69	–	–	100.22	
–	–	–	–	46.89	–	–	–	–	–	30.77	22.35	–	–	100.01	

(Fig. 4b) and aqueous-carbonic liquid-rich inclusions (Lwc) (Fig. 4c).

The primary inclusions form the first (I) FI syngenetic assemblage (Table 8).

Aqueous liquid-rich inclusions (Lw) are abundant and consist of two phases: vapor and liquid, with the vapor phase proportion varying from 10 to 40 vol% at room temperature. The size of these inclusions ranges

from 2 to 40 μm with an average size of ~10 μm. The common shapes of Lw-type inclusions are rounded and they also show negative crystals shapes. The Lw-type inclusions were found in assemblages together with Vw-type inclusions or with Lwc-type inclusions.

Aqueous vapor-rich inclusions (Vw) consist of > 70 vol% vapor and < 30 vol% liquid water. Vw-type inclusions have oval, rounded

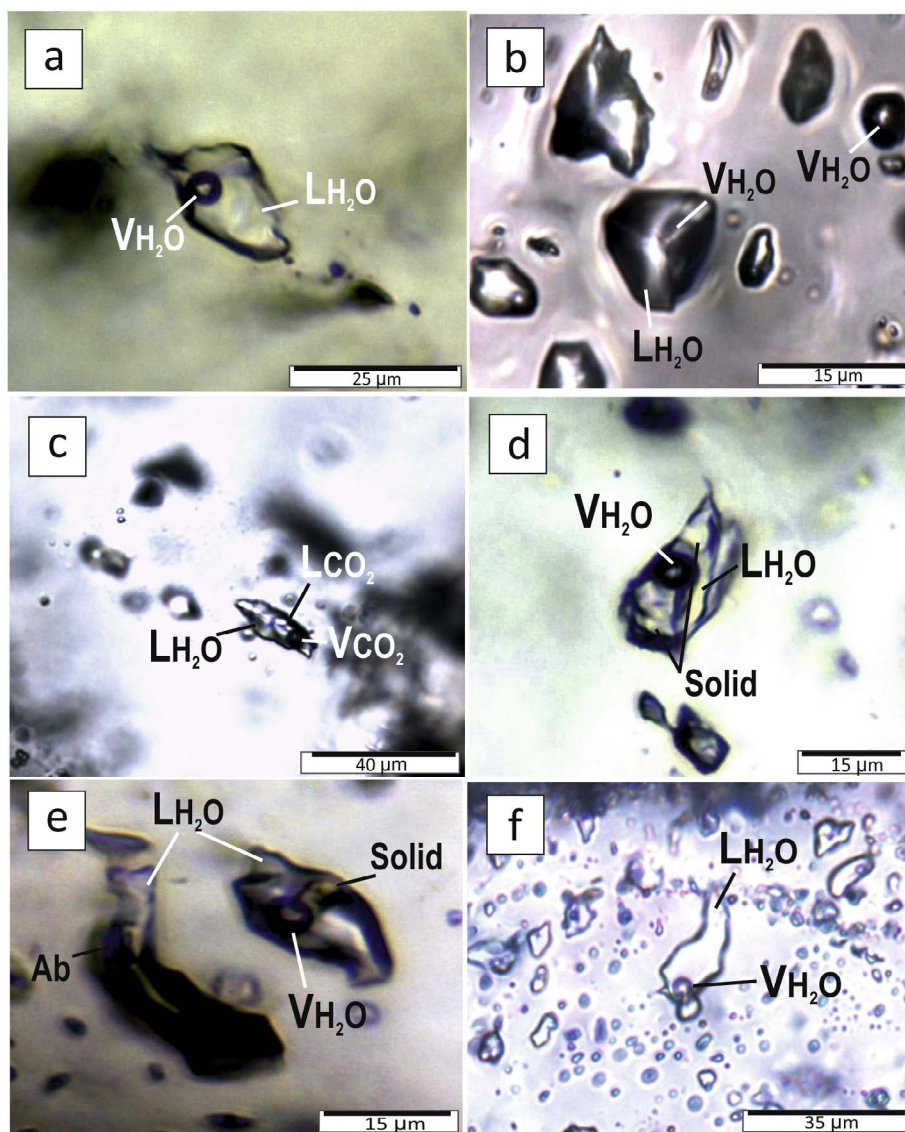


Fig. 4. Photomicrographs of fluid inclusions in quartz from ore veins of the Rogovik deposit: (a) primary Lw-type fluid inclusions in early-stage quartz; (b) primary Vw-type fluid inclusions coexist with Lw-type fluid inclusions in early-stage quartz; (c) primary Lwc-type fluid inclusions in early-stage quartz; (d, e) pseudosecondary LVS-type fluid inclusions in late-stage quartz; (f) pseudosecondary and secondary Lw-type fluid inclusions in late-stage quartz. Abbreviation: V_{CO_2} , vapor CO_2 ; L_{CO_2} , liquid CO_2 ; V_{H_2O} , vapor H_2O ; L_{H_2O} , liquid H_2O ; Solid, solid phase.

and negative crystals shapes, and range from 10 to 20 μm in size. They with primary Lw-type inclusions occur in the center of quartz grains (Fig. 4b).

Aqueous-carbonic liquid-rich inclusions (Lwc) are generally rare (Fig. 4c). These are three-phase CO_2 -bearing inclusions with an aqueous liquid phase and a vapor bubble with a double meniscus of CO_2 liquid ($L_{H_2O} + L_{CO_2} + V_{CO_2}$). The CO_2 liquid phase proportions of the inclusions at room temperature vary from 20 to 40 vol%. The shapes of Lwc-type inclusions are irregular and elongated and their size ranges from 15 to 30 μm .

We have classified the pseudosecondary inclusions of quartz grains from adularia-quartz aggregates as the second (II) FI assemblages (Table 8). These are scarce Lw-type inclusions and occur in healed fractures limited by the outside growth zones of quartz. They consist of two phases: vapor and liquid, with the vapor phase proportion varying from 10 to 20 vol% at room temperature, and have rounded shapes and average size of 20 μm . These inclusions do not form assemblages with other types of FI and are responsible for the silver-bearing mineralization of Au-Ag ore zones, which occurs as the healed microveinlets in the quartz grains.

There are numerous secondary aqueous liquid-rich and vapor-rich inclusions arranged along cross-cutting fractures and planes in gangue minerals of the early ore-forming stage. Extremely small dimensions

hamper diagnosis of FI composition. These inclusions are related to later ore-forming processes and confirm heterogenization and boiling of ore-bearing fluids.

The mineralization in the quartz grains from the quartz-albite (orthoclase)-carbonate aggregates of the late ore-forming stages forms disseminated micro-veinlets and elongated aggregates filling the microcracks in the gangue minerals. So, we focused our study on the pseudosecondary and secondary fluid inclusions. Two types of fluid inclusions were identified at room temperature in these quartz-albite (orthoclase)-carbonate aggregates: aqueous liquid-rich inclusions (Lw) (Fig. 4f) and polyphase inclusions (LVS) (Fig. 4d and e).

The Lw-type fluid inclusions consist of two phases: vapor and liquid, with the vapor phase proportion varying from 10 to 20 vol% at room temperature. These inclusions have irregular and oval shapes, and range from 10 to 30 μm in size. The Lw-type inclusions were found in the assemblages together with LVS-type inclusions. The inclusions fill the healed cracks of the gangue minerals with Ag-Pb mineralization and form the third (III) FI syngenetic assemblage (Table 8).

The LVS fluid inclusions are also associated with secondary Lw-type fluid inclusions filling the plains and microcracks of the gangue minerals with the late Ag-Au-Pb mineralization (IV FI assemblage, Table 8). The polyphase (LVS) three-phase fluid inclusions contain an aqueous liquid phase, a vapor bubble and a presumably

Table 8
Microthermometric and Raman data of fluid inclusions in quartz from the Rogovik deposit.

Types of ore mineral assemblages	Type of FI, syngenetic assemblage	Depth, m	Type of FI (composition)	T, °C					NaCl-eq., %	Composition	Gas phase, mol.%			Solid phase	
				T _h	T _m	T _{m,Clt}	T _{h,CO2}	T _{eut}			Solution	CO ₂	CH ₄		H ₂
<i>Early volcanic stage</i>															
Au-Ag	Primary	20	Lw	200–300	–0.3... –4.3	—	—	–50... –45	0.5–6.9	CaCl ₂ - NaCl- H ₂ O	76.8–78.4	21.6–23.2	—	—	
			Vw	250–275	–1.4... –2.3	—	—	—	2.4–3.9	—	—	—	—	—	
	Lw	80.9–81.1	270–300	–3... –2	—	—	–45... –40	3.4–4.9	CaCl ₂ - NaCl- H ₂ O	58.3–62.4	11.5–19.3	18.4–30.2	—		
		Lwc	280–290	—	–3... –2.9	23.0.33	–45... –35	3.7–3.8	H ₂ O	65.4–70.1	14.2–16.4	13.5–20.4	—		
Pseudo-secondary II	20	Lw	90–190	–0.7... –4	—	—	–50... –45	1.2–6.4	CaCl ₂ - NaCl- H ₂ O	—	—	—	—		
			<i>Late volcanoplutonic stage</i>												
Ag-Pb	Pseudo-secondary III	170	Lw	195–220	—	—	—	—	—	—	100	—	—		
		100	Lw LVS	140–200	–7... –2	—	—	–25... –11	3.4–10.5	KCl- NaCl- H ₂ O	0.1–34.8	65.2–99.9	—	—	
Ag-Au-Pb	Pseudo-secondary and secondary IV	148.5	Lw	120–235	–5... –4.8	—	—	–24... –15	7.6–7.9	KCl- NaCl- H ₂ O	0.1–32.2	67.8–99.9	—	—	
		260.5	LVS	150–180	–1.0	—	—	—	0.1–1.7	—	—	95–100	5–0	Ab	

Notes: Homogenization temperatures (vapor disappearance, T_h; CO₂ meniscus disappearance, T_{h,CO2}), final melting temperatures of clathrate (T_{m,Clt}), final ice melting temperatures (T_m) and eutectics temperatures (temperature of the lowest melting point, T_{eut}). — - parameter not determined.

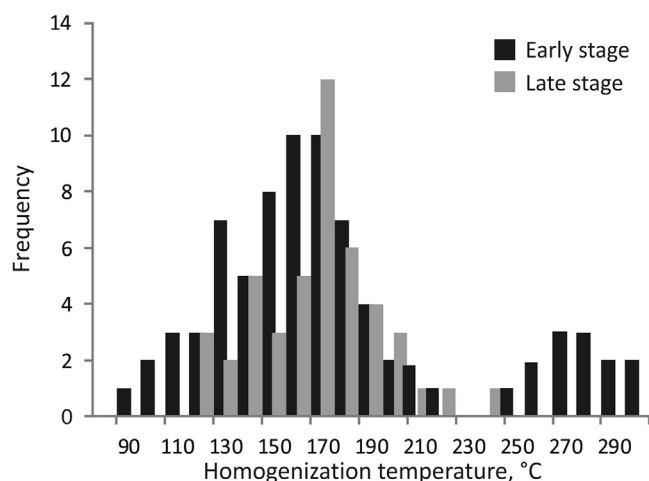


Fig. 5. Histograms of homogenization temperatures of fluid inclusions for the early volcanic (1) and late volcanoplutonic (2) stages of mineralization at the Rogovik deposit.

heterogeneously trapped solid phase albite. LVS and Lw FI, have irregular shapes and sizes ranging from 20 to 50 μm. Pseudosecondary LVS-inclusions occur in the outside growth zones of quartz grains and secondary inclusions align along micro-fractures and planes.

4.2. Microthermometric and Raman results

The microthermometric and Raman data, summarized in Table 8, were obtained from Lwc-, Lw-, Vw- and LVS-type fluid inclusions of the both ore-forming stages.

The *early volcanic stage* quartz crystals contain dominantly Lw-type and Vw-type with rare Lwc-type fluid inclusions (the I FI assemblage). Associated with Vw-type inclusions the Lw-type fluid inclusions have the first ice melting temperature (T_{eut}) range of –50 to –45 °C, this data suggests the presence of CaCl₂ and NaCl in the hydrothermal solution (Borisenko, 1977; Steele-MacInnis et al., 2011). The final ice

melting temperatures (T_m) are between –0.3 and –4.3 °C, which correspond to salinities between 0.5 and 6.9 wt% NaCl-eq. These inclusions are homogenized to the liquid phase at temperature (T_h) between 200 and 300 °C (Fig. 5). Raman data show that the gas phases of both type inclusions consist of CO₂ (~78 mol.%) and CH₄ (~22 mol.%) (Table 8).

The measured eutectic temperatures documented in the Lw-type fluid inclusions occurred in an assemblage with Lwc-type inclusions average –45...–40 °C, which are correlated with the CaCl₂-NaCl-bearing hydrothermal fluid system (Borisenko, 1977; Steele-MacInnis et al., 2011). These inclusions have the final ice melting temperature (T_m) range of –3 to –2 °C indicating an average salinity of 3.4–4.9 wt % NaCl-eq. The inclusions homogenize to a liquid phase at temperature ranging from 270 to 300 °C (Fig. 5). Raman data show that the gas phase of these inclusions consists of CO₂ (58.3–62.4 mol.%), CH₄ (11.5–19.3 mol.%) and H₂ (18.4–30.2 mol.%) (Table 8). The Lwc-type fluid inclusions have the final melting temperature range of clathrate (T_{m,Clt}) of –3 to –2.9 °C indicating the low average salinity of 4.8–4.9 wt% NaCl-eq. In these inclusions, the measured temperatures of the CO₂ phase homogenization (T_{h,CO2}) to a vapor phase are 23–33 °C. Raman data show that the gas phases of Lwc-type inclusions consist of CO₂ (65.4–70.1 mol.%), CH₄ (14.2–16.4 mol.%) and H₂ (13.5–20.4 mol.%) (Table 8, Fig. 6).

Pseudosecondary Lw-type fluid inclusions (the II FI association) have the eutectic temperatures (T_{eut}) range of –50 to –45 °C, this data set correlates with a CaCl₂-NaCl-bearing hydrothermal fluid system (Borisenko, 1977; Steele-MacInnis et al., 2011). The final ice melting temperatures (T_m) range from –4 to –0.7 °C, which indicates a salinity of 1.2–6.4 wt% NaCl-eq. Pseudosecondary Lw-type fluid inclusions are homogenized to liquid at temperatures (T_h) from 90 to 190 °C (Fig. 5).

The *late volcanoplutonic* Ag-Pb stage quartz crystals contain dominantly Lw- and LVS-type fluid inclusions of the III FI syngenetic assemblage (Table 8). The first ice melting temperature (T_{eut}) for the Lw-type fluid inclusions ranges from –25 to –11 °C, this data set correlates with the KCl-NaCl-bearing hydrothermal fluid system (Borisenko, 1977). The final ice melting temperatures (T_m) are between –7 and –2 °C, which correspond to salinities of 3.4 and 10.5 wt% NaCl-eq. The

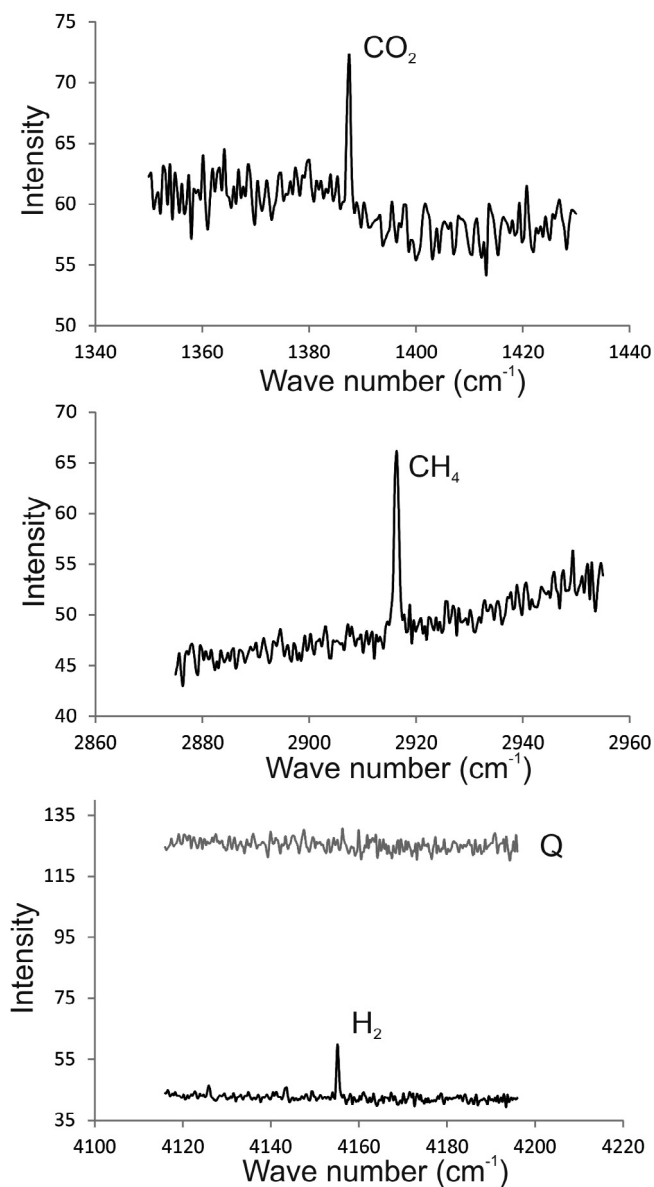


Fig. 6. Representative Raman spectra, showing the gas composition of Lwc-type fluid inclusion in quartz grains from adularia-quartz aggregates formed at the early stage.

inclusions homogenize to the liquid phase at temperature ranging from 140 to 220 °C, with a mean mode at 180 °C (Fig. 5). Raman data show that the gas phases of these inclusions consist of CH₄ (65.2–99.9 mol.%) and CO₂ (0.1–34.8 mol.%) (Table 8).

The pseudosecondary and secondary Lw inclusions of the late Ag-Au-Pb mineralization (the IV FI assemblage) have the first ice melting temperature (T_{emf}) of -24 to -15 °C, this data set correlates with the KCl-NaCl-bearing hydrothermal fluid system (Borisenko, 1977) (Table 8). The final ice melting temperature for these inclusions ranges from -5 to -4.8 °C, which corresponds to salinities from 7.6 to 7.9 wt % NaCl-eq. These fluid inclusions homogenized at temperatures (T_h) of 120–235 °C. Gas analyses show CH₄ (67.8–99.9 mol.%) with less CO₂ (0.1–32.2 mol.%). Secondary LVS-inclusions have the final ice melting temperature (T_m) range of -1 to 0 °C, this data set indicates the low salinity of 0.1–1.7 wt% NaCl-eq. In these inclusions the measured temperatures of the vapor disappearance (T_h) are 150–180 °C. After vapor disappearance, solid phase remains at a further increase of temperature. This is the evidence of the probable trap of crystals. Raman data show that the solid phases consist of prismatic

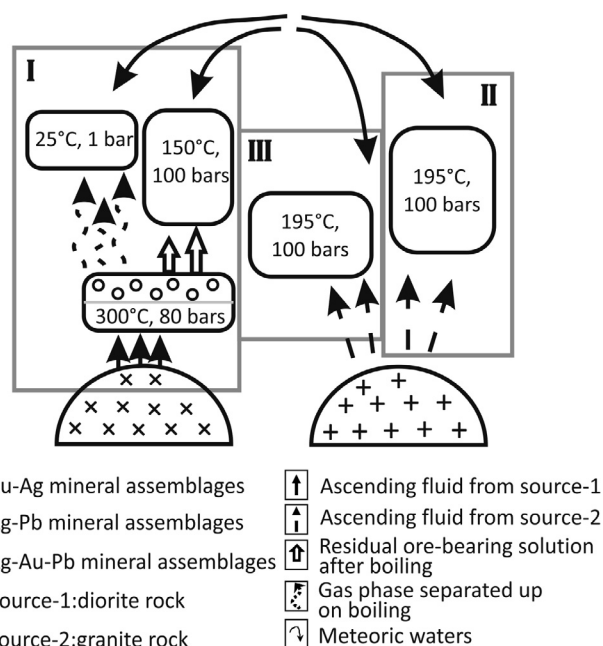


Fig. 7. Sketch of the formation stages of the Rogovik deposit summarizing the modeled scenarios.

heterogeneously trapped albite crystals. Gas analyses show CH₄ (95–100 mol.%) with less H₂ (0–5 mol.%).

5. Thermodynamic modeling

In modeling we took into account the fact that the Rogovik deposit was formed during two stages (Table 4) with different T,P-conditions, mineral assemblages and ore metal endowments (especially Au, Ag, Hg and S). Mineralogical studies show that the most typical assemblages for the early stage are the pyrite-electrum-naumannite and the gold-acanthite-naumannite mineral assemblages hosted by adularia-quartz veins. Ag-sulfosalts with naumannite in the zones of sericite-quartz veinlets and pyrite-galena-Ag-sulfosalts-Ag-sulfoselenides mineral assemblages in quartz-albite(orthoclase)-carbonate aggregates are abundant at the late stage. Microthermometry results of fluid inclusions of the early stage showed two mean modes at ~ 270 and ~ 160 °C, for the geochemical modeling a range of temperatures between 150 and 300 °C was therefore assumed. For the late stage the average homogenization temperature was ~ 180 °C and in the geochemical modeling calculations we used 195 °C. As the Rogovik is an epithermal deposit formed at shallow depths, the predicted pressure for deposits of this class does not exceed 80–100 bar (White and Hedenquist, 1990). To simplify the calculations in the titration models, we took the pressure of 100 bar.

Different scenarios for the formation of the Au-Ag, Ag-Pb and Ag-Au-Pb mineral assemblages at the Rogovik deposit were modeled, which are schematically described in Fig. 7. For the Au-Ag mineral assemblage associated with the early volcanic ore-forming stage, the following scenarios were modeled: model of boiling solution genetically related to a deep-seated diorite massif, model of mixing of a gas phase with meteoric waters and the model of residual solution and host rock interaction. For the late ore-forming stage, we modeled the formation of “silver mineralization” using an ore-forming solution genetically related to a deep-seated granite massif and interacting with host rocks and gold-silver ores of the early volcanic ore-forming stage.

5.1. Early volcanic stage: Au-Ag mineral assemblage

The composition of the first model solution was equilibrated with diorite of an average composition (Kravtsova, 2010) from the OCVB

Table 9Compositions of rocks calculated in molar quantities of elements in 1 kg of rock and compositions of solutions (mol/kg H₂O) used in model calculations.

Element	Diorite	Granit	Ignimbrite	Au-Ag ores	Solution-1	Residual solution	Solution-2
Si	8.788	12.248	12.234	–	3.09E–02	7.30E–03	1.78E–02
Ti	0.163	0.026	0.029	–	0.00E+00	0.00E+00	0.00E+00
Al	3.378	2.583	1.358	–	3.37E–08	1.58E–07	9.32E–08
Fe	1.113	0.359	0.312	–	1.20E–05	5.64E–05	8.06E–04
Mn	0.039	0.007	0.019	–	8.80E–02	4.14E–01	1.08E+00
Mg	0.844	0.074	0.067	–	1.85E–06	8.70E–06	1.42E–04
Ca	1.405	0.207	0.091	–	1.87E–03	8.79E–03	5.61E–03
Na	1.026	1.165	0.269	–	2.05E–01	9.64E–01	3.97E–01
K	0.295	0.093	0.624	–	4.37E–02	2.05E–01	2.50E–02
S	7.98E–03	6.86E–03	–	1.87E–02	4.62E–02	3.07E–03	2.52E–02
Se	1.62E–06	7.98E–06	–	1.62E–05	3.38E–05	8.43E–05	9.41E–06
Ag	1.58E–06	8.90E–06	–	2.78E–05	2.01E–06	1.52E–07	8.65E–05
Cu	6.61E–04	1.42E–04	–	1.57E–05	4.86E–05	2.29E–04	3.92E–08
Zn	1.56E–03	5.81E–04	–	3.06E–05	2.36E–06	1.11E–05	2.17E–04
As	1.25E–04	3.60E–04	–	2.67E–04	2.05E–14	8.53E–14	1.29E–04
Pb	1.16E–04	1.54E–04	–	3.86E–06	4.54E–06	2.13E–05	1.34E–04
Sb	4.93E–06	2.46E–04	–	2.46E–05	4.85E–14	2.28E–13	1.43E–04
Au	1.52E–08	5.58E–09	–	3.73E–06	8.30E–08	1.10E–07	2.76E–08
Hg	1.68E–08	1.58E–04	–	1.68E–06	6.41E–07	1.63E–10	1.68E–05
Cl	1.11E–02	1.59E–02	–	–	4.25E–01	2.00E+00	2.59E+00
C	4.10E–02	1.28E–01	–	–	9.83E–02	1.00E–03	2.62E–01

which was selected from Table 9. Thermodynamic equilibrium of “diorite-water” interaction was calculated at a temperature of 400 °C and pressure 450 bar. A titration set up was used to model different rock/water (R/W) ratios at which the composition of model solution 1 becomes substantially enriched in Ag, Se, S, Hg and Au. This corresponds to the “rock-dominant” regime with a R/W = 25 (Table 9).

Model of boiling: The model is based on the assumption that, during the ascent of the ore forming solution into a fractured zone, partial boiling of the hydrothermal solution takes place when pressure drops to the pressure of saturated vapor. The model does not consider interaction of the hydrothermal fluid with wall rocks. As a result of boiling, a gas phase and a residual hydrothermal solution are formed. The gas phase rises to more shallow depth and mixes with meteoric water, and the residual solution reacts with the host rock (ignimbrite), which are modeled separately. This scenario of boiling was calculated with the help of the reactive transport code provided in the Selektor-C software packages. Model solution-1 is used as the initial solution composition. Partial boiling of hydrothermal solution-1 takes place under the conditions of isobaric-isothermal system at T = 300 °C and P = 80 bar, the set pressure is somewhat lower than the pressure on the liquid vapor curve at this temperature. The residual hydrothermal solution remaining after boiling is given in Table 9.

The calculations showed that the modeled gas-vapor phase contains H₂, CO₂, H₂S and CH₄. Partial boiling is followed by fractionation of the main part of Hg and Se into a gas phase, with a considerable quantity of Ag, Pb, As and Sb being concentrated in the residual hydrothermal solution. The calculations showed that in the conditions of stationary degassing of the ascending flow Au, Ag and Se can deposit to form electrum, naumannite and quartz.

Model of mixing of ore-bearing gas phase with meteoric water: The gas phase, separated up on boiling of the model solution 1, ascends and interacts with meteoric water saturated with atmospheric oxygen and carbon dioxide (T = 25 °C and p = 1 bar) without reacting with host rocks.

As a result of mixing of ore-bearing gas phase with meteoric water, the solutions are acidified, oxygen fugacity (fO₂) in the system increases, and high-fineness gold (composition Ag_{0.36}Au_{0.64}, fineness 780‰), naumannite, cinnabar and graphite are deposited. The deposition process of Au depends on the ratio “meteoric water/gas phase” (MW/G). The calculations showed that deposition of Au in association with mercury sulfide and graphite proceeds at rather high dilution –

MW/G = 2.5:1–40:1, and that of naumannite in the same association, at lower dilution – MW/G = 0.01:1–0.025:1.

The model of interaction of the residual solution with host rocks is as follows. The calculation of equilibria is based on the method of the extent of reaction (titration model) where the increasing rock/water (R/W) ratio represents subsequent water–rock interaction. Partial equilibrium states at the low values of this ratio are represented by the most altered parts of rocks (Borisov, 2000). In the model calculations we specified the interactions of different portions of host rocks (R/W from 10^{–2} to 100) with 1 kg residual solution at temperature of 150 °C and pressure of 100 bar.

Fig. 8 shows the results of modeling of compositions of calculated mineral assemblages and aqueous solutions. The main rock-forming minerals are orthoclase, albite, quartz, chlorite and muscovite, and at R/W > 4 carbonate starts forming (Fig. 8a). The total quantity of minerals ruling out rock-forming minerals at R/W > 7 is no more than 0.7%, and it is 3% at R/W < 7. Base-metal sulfides are represented by galena, chalcopyrite, sphalerite and pyrite (Fig. 8b). Solid solutions Au–Ag–Hg are represented by Hg-bearing high-fineness gold (Ag_{0.008}Au_{0.99}Hg_{0.002}) at R/W > 3 and electrum (Ag_{0.502}Au_{0.495}Hg_{0.003}) at R/W < 3. At specified concentrations of Au, Ag, S and Se in the system, naumannite appears at R/W < 0.3, whereas gold amalgams precipitate across the entire range of R/W.

The resulting ore-forming solution formed by the interaction of ignimbrite-residual solution is neutral, its pH varies from 6.7 to 7.7 (Fig. 8c). Maximum concentrations of Ag, Au and Hg reach 2.3·10^{–9}, 9.1·10^{–10} and 2.96·10^{–9} mol/1 kg H₂O (Fig. 8c), respectively. The modeling results show that the main forms of transfer of ore components in the aqueous solution are: dihydrosulfide complexes Ag(HS)₂[–] and Au(HS)₂[–] for Ag (Fig. 8d) and Au (Fig. 8e); sulfide complex HgS(HS)[–] for Hg (Fig. 8f).

5.2. Late volcanoplutonic stage: Ag–Pb mineral assemblage

To determine the composition of ore-bearing solution 2 (Table 9) of the late stage, we analyzed the interaction of 1 kg granite (Table 9) with pure water at a temperature of 400 °C and a pressure of 450 bar. The titration model allowed us to choose the required rock/water (R/W) ratio at which the solution composition becomes substantially enriched in Ag, Pb, Zn, Hg, S, Se, As and Sb. This corresponds to the “rock-dominant” regime of R/W = 15.

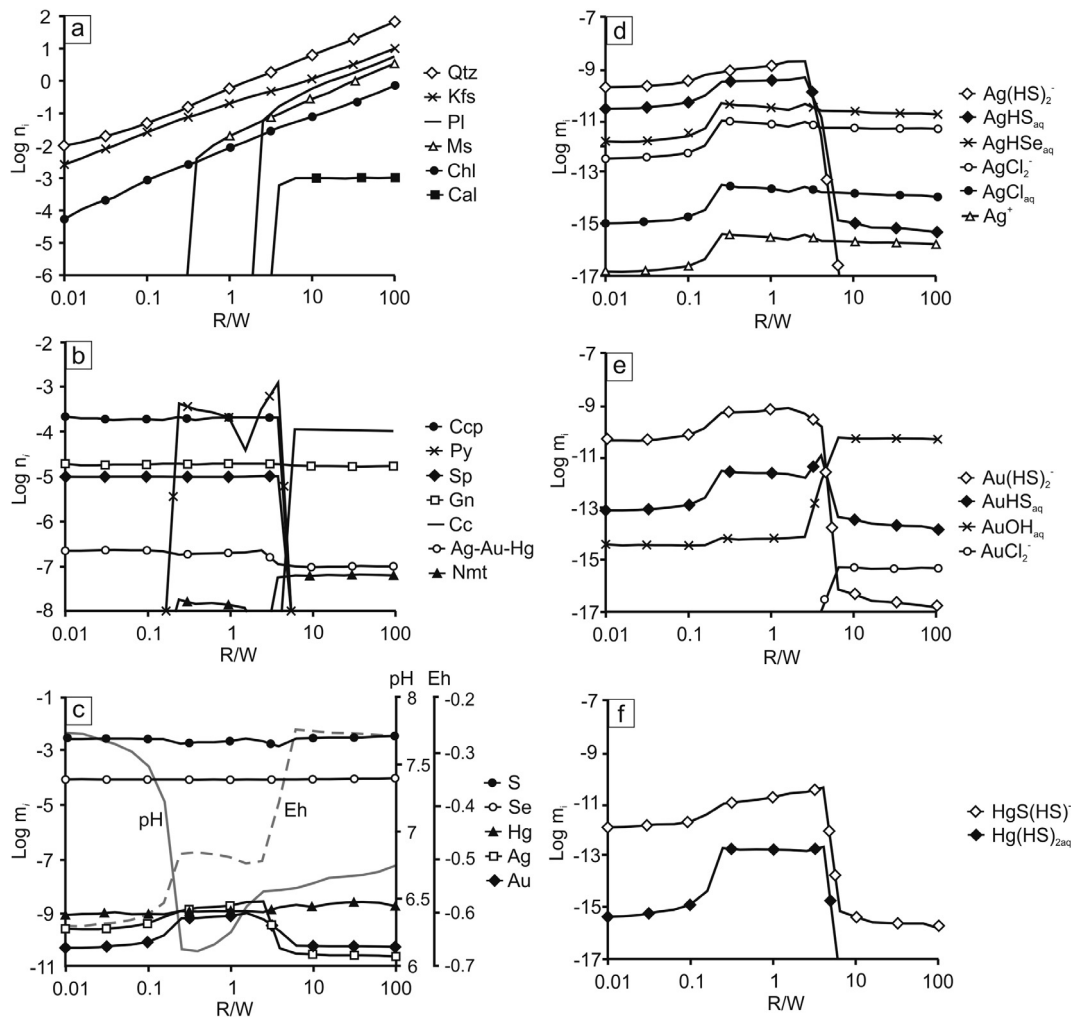


Fig. 8. Geochemical modeling results for the formation of Au-Ag mineral assemblages of the early volcanic stage. The interaction of residual ore-bearing solution with host rocks is represented by increasing R/W. (a) Modeled gangue and (b) ore mineral assemblages of Au-Ag ore mineral assemblages. (c) Total concentrations of S, Se, Au, Ag and Hg in solution; d-f. Concentrations of (d) Ag, (e) Au, and (f) Hg species in solution. n – molal amount of solid component; m – molal amount of aqueous component; Qtz – quartz; Kfs – K-feldspar; Pl – plagioclase; Ms – muscovite; Chl – chlorite; Cal – calcite; Py – pyrite; Sp – sphalerite; Gn – galena; Ccp – chalcocopyrite; Cc – chalcocite; Nmt – naumannite; Ag-Au-Hg – solid solution.

At this stage of development of the ore-forming process, at temperature 195 °C and pressure 100 bars, model solution-2 interacts with host rocks. In the calculations, different portions of host rocks (R/W from 10^{-3} to 10) and 1 kg hydrothermal solution-2 were specified.

The modeling results show that the main rock-forming minerals are quartz, carbonate, muscovite and at R/W > 0.4 chlorite and orthoclase appear (Fig. 9a). The base-metal sulfides are pyrite, sphalerite, galena, at R/W < 0.4 cinnabar is stable in association with arsenopyrite, and at R/W > 5 chalcocopyrite is stable (Fig. 9b). The amount of pyrite gradually increases, and the ratios between sphalerite and galena remain constant. Silver minerals are silver amalgams ($Ag_{0.80}Hg_{0.20}$ and $Ag_{0.65}Au_{0.12}Hg_{0.23}$), Se-acanthite and S-naumannite. The formation of kustelite depends on the decrease in concentrations of H_2S in the solution at ratio R/W = 0.25.

The composition of modeled silver sulfoselenides is diverse. The results of calculations showed that the first to precipitate from the solution at R/W < 0.4 is the phase enriched in sulfur ($Ag_{2.5}S_{0.78}Se_{0.22}$), and at R/W > 0.4 naumannite starts to form, the content of S in which is less than 0.1 M fraction.

The calculations show that pH of the ore-bearing solution, with increasing R/W, changes from weak-acid to neutral (Fig. 9c). The maximum contents of Au, Ag, Hg and S in the solution were detected at R/W < 0.4 (Fig. 9c). The role of main carriers of ore elements in the solution changes with its infiltration (Fig. 9d–f): at R/W < 0.4, the

main species of transfer of Au, Ag and Hg are their different sulfur complexes ($Au(HS)_2^-$, $Ag(HS)_2^-$, $AgHS_{aq}$, $HgS(HS)^-$, $Hg(HS)_{2aq}$); at R/W 0.4–1.6, Ag is transferred mainly by the chloride complex $AgCl_2^-$, Au and Hg also by hydrosulfide complexes but its concentrations in the solution drop drastically; at R/W > 1.6, dihydrosulfide complex of silver $Ag(HS)_2^-$ is predominant.

5.3. Late volcanoplutonic stage: Ag-Au-Pb mineral assemblage

The model of formation of Ag-Au-Pb mineralization is based on the interaction of ore-bearing solution-2 with Au-Ag mineral assemblage of the early stage (Table 9) at temperature 195 °C and pressure 100 bar. In the model calculations we took 1 kg of solution-2 and different portions of minerals of the early stage (R/W from 10^{-3} to 10), in which the concentrations of ore and accompanying elements are specified on the basis of their contents in Au-Ag mineral assemblage from the deposit.

As a result, during the infiltration of the solution at low R/W muscovite and quartz form as the main gangue phases (Fig. 10a) and pyrite, sphalerite, galena, cinnabar, silver sulfoselenides of the acanthite series and fahlores as the main ore minerals (Fig. 10b). With increasing R/W albite, K-feldspar, chlorite and calcite appear and the content of sulfides – pyrite, sphalerite, and galena – during the processes increases. Arsenopyrite precipitates at R/W > 0.04. Solid solution Au-Ag-Hg precipitates at R/W > 0.03. Au and Ag minerals are mercuric

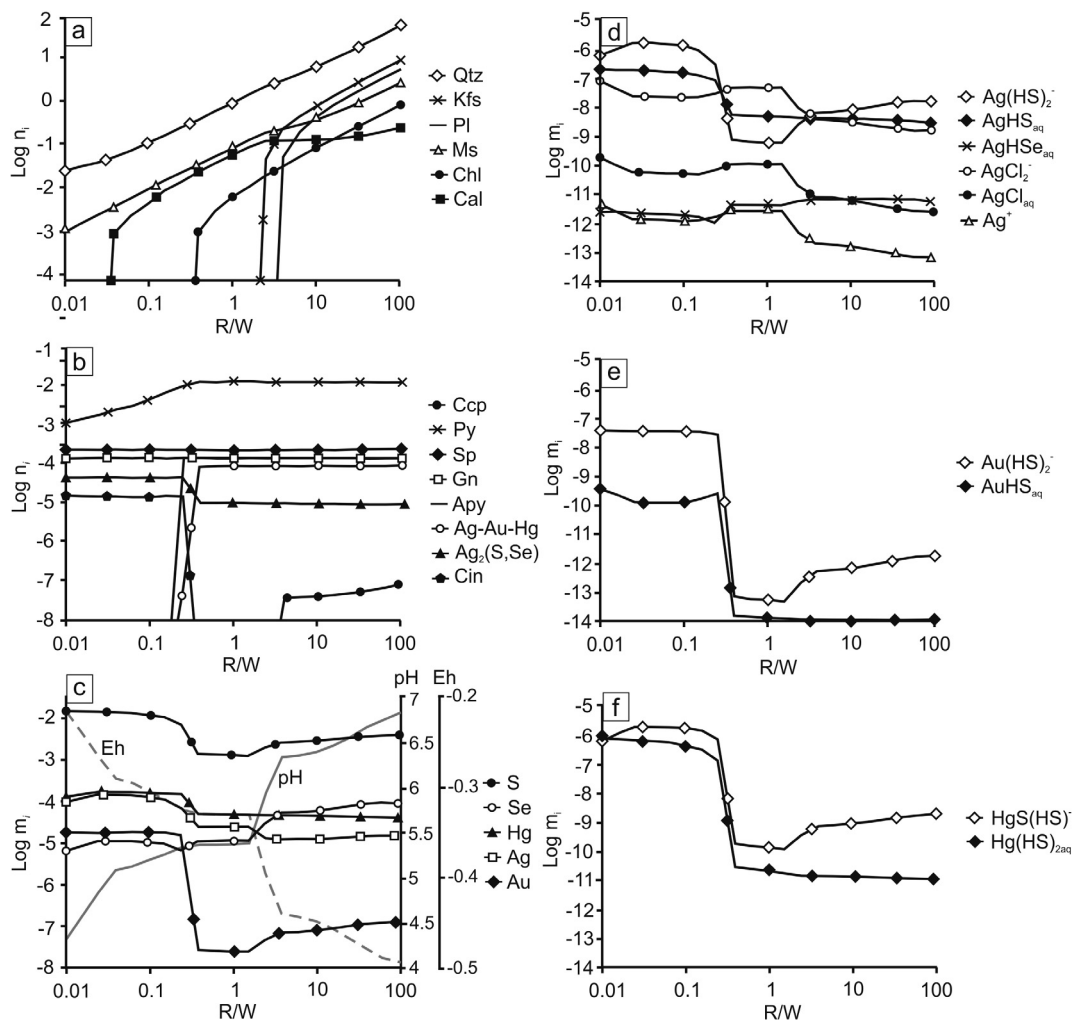


Fig. 9. Geochemical modeling results for the formation of Ag-Pb mineral assemblages of the late volcanoplutonic stage. The interaction of ore-bearing solution-2 with host rocks is represented by increasing R/W. (a) Modeled gangue and (b) ore mineral assemblages of Ag-Pb ore mineral assemblages. (c) Total concentrations of S, Se, Au, Ag and Hg in solution; d-f. Concentrations of (d) Ag, (e) Au, and (f) Hg species in solution. n – molal amount of solid component; m – molal amount of aqueous component; Qtz – quartz; Kfs – K-feldspar; Pl – plagioclase; Ms. – muscovite; Chl – chlorite; Cal – calcite; Py – pyrite; Sp – sphalerite; Gn – galena; Ccp – chalcocopyrite; Apy – arsenopyrite; Cin – cinnabar; Ag₂(S,Se), Ag-Au-Hg – solid solutions.

high-finesness gold (Ag_{0.03}Au_{0.75}Hg_{0.22}–Ag_{0.10}Au_{0.72}Hg_{0.18}), electrum (Ag_{0.54}Au_{0.35}Hg_{0.11}–Ag_{0.60}Au_{0.16}Hg_{0.24}), kustelite (Ag_{0.77}Au_{0.02}Hg_{0.21}–Ag_{0.67}Au_{0.11}Hg_{0.22}) (Fig. 10c) and silver sulfoselenides.

The calculations showed that the hydrothermal solution becomes neutral (pH changes with the interval 4.5–7). The concentration of dissolved Ag gradually decreases, whereas Hg decreases by an order of magnitude at R/W 0.04–1, which directly results in discontinuation of cinnabar precipitation. The role of main carriers of ore elements in the solution changes with its infiltration (Fig. 10d–f): the solutions are weakly acidic (pH = 4–5) and the main forms of transfer of gold, silver and mercury are their different sulfur complexes (Au(HS)₂⁻, Ag(HS)₂⁻, AgHS_{aq}, HgS(HS)⁻, Hg(HS)_{2aq}); at R/W > 0.025 concentrations of these hydrosulfide complexes decrease.

6. Discussion

Results of thermodynamic calculations using different models explain some regularities in the formation of different types of ore mineral assemblage from the Rogovik deposit. On partial boiling, there forms a gas-vapor phase enriched with volatile and ore components, which through pores and cracks penetrates the above-lying levels, being condensed on the impermeable barriers on the way of migration or reaching near-surface areas. The calculations showed that the modeled

gas-vapor phase contains H₂, CO₂, H₂S and CH₄. Microthermometric and Raman results confirm the presence of H₂ (up to 30 mol.%) in the gas mixture of primary fluid inclusions, but the H₂S was not established in them. The calculations showed that electrum, naumannite and quartz can form under the conditions of partial boiling. This mechanism explains the occurrence of fine-dispersed naumannite in Au-Ag mineral assemblages of the early stage and, in addition, supports the hypothesis of the colloid mechanism of formation of these minerals or the transfer of elements by a gas mixture (Saunders et al., 2008; Hurtig and Williams-Jones, 2015). The evidence in favor of the boiling process of hydrothermal fluid comes from fluid inclusions study, namely the presence of the first (I) fluid inclusion assemblage in quartz of the early stage.

The modeling calculations of mixing of the ore-bearing gas phase with meteoric water showed that, according to the model, a high-finesness gold + naumannite + cinnabar + graphite assemblage is formed. Results of mineralogical studies showed that among the minerals of Au-Ag mineral assemblages no high-finesness gold and cinnabar were found and, therefore, this mixing model does not provide a full description of the mineralogy of Au-Ag mineral assemblages. The formation of typical Au-Ag mineral assemblages can be interpreted using the model of interaction of the residual aqueous solution with host rocks. The model describes mineral formation from the cooled

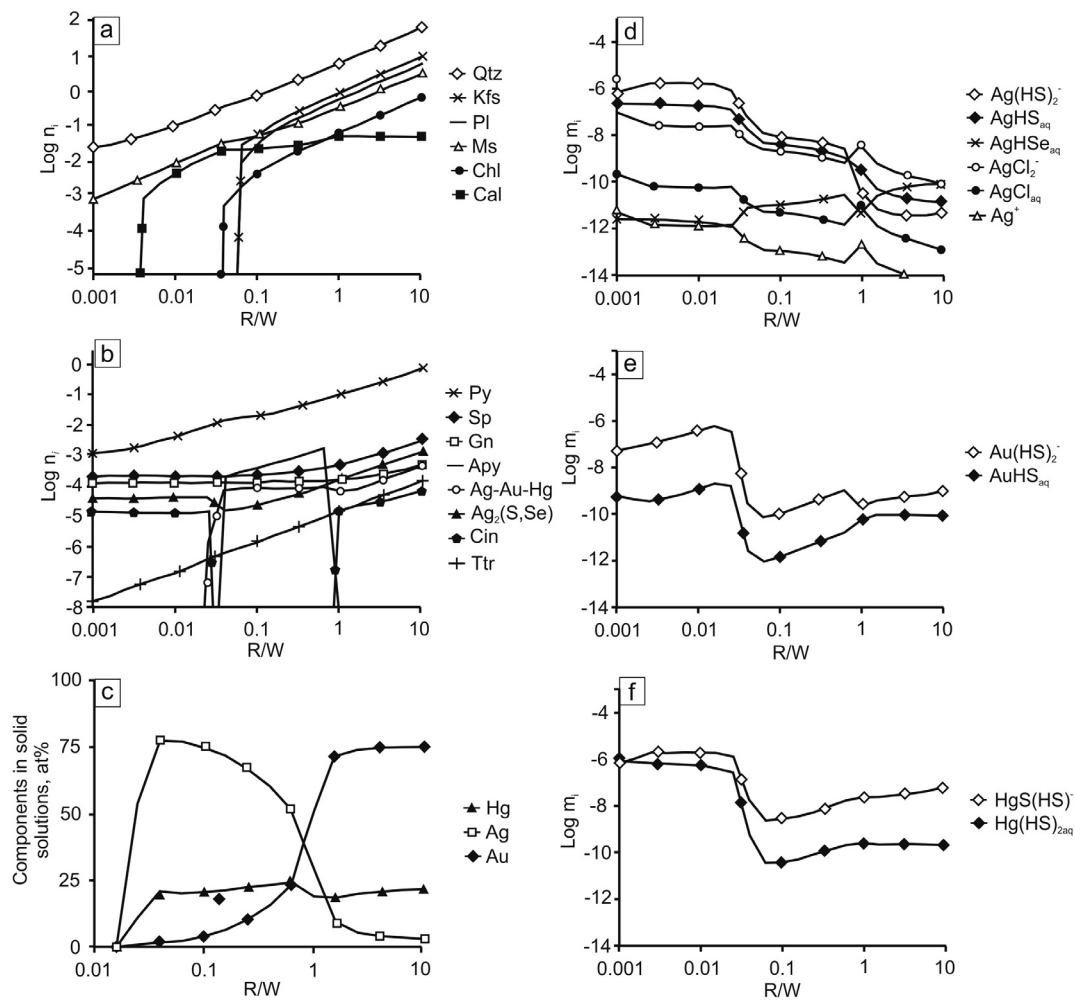


Fig. 10. Geochemical modeling results for the formation of Ag-Au-Pb mineral assemblages of the late volcanoplutonic stage. The interaction of ore-bearing solution-2 with Au-Ag mineralized zones is represented by increasing R/W. (a) Modeled gangue and (b) ore mineral assemblages of Ag-Au-Pb ore mineral assemblages. (c) Calculated compositions of Ag-Au-Hg solid solutions; d-f. Concentrations of (d) Ag, (e) Au, and (f) Hg species in solution. n – molal amount of solid component; m – molal amount of aqueous component; Qtz – quartz; Kfs – K-feldspar; Pl – plagioclase; Ms – muscovite; Chl – chlorite; Cal – calcite; Py – pyrite; Sp – sphalerite; Gn – galena; Apy – arsenopyrite; Ttr – tetrahedrite; Cin – cinnabar; $Ag_2(S,Se)$, Ag-Au-Hg – solid solutions.

solution at different R/W ratios and characterizes the low-temperature mode 160–170 °C at the early stage (Fig. 5). By comparing the results of modeling and mineralogical study, we can define possible R/W ratios achieved during ore formation at the Rogovik deposit. The coexistence of pyrite + sphalerite + galena + naumannite is consistent with the range of specific values of R/W ratios of 0.3–3 (Fig. 8b).

Our calculations support an assumption that the formation of considerable amounts of gold at the deposits with multistage mineralization (Volkov, 2005) is only probable in the presence of two combined processes. These processes are: boiling of high-temperature fluids under the shield of volcanogenic series and further mixing of a magmatic fluid with meteoric waters nearby the zones of structural discordance where rapid cooling of ore-forming solutions are likely.

Formation of Ag-Pb mineral assemblage of the late volcanoplutonic stage were modeled by interacting the ore-forming aqueous solution-2 with host rocks. The calculations showed that on the basis of this model the pyrite + sphalerite + galena + naumannite + native silver assemblage is formed, which is consistent with the mineralogical study. This model describes wide variations in the compositions of silver sulfoselenides of acanthite series ($Ag_2S-Ag_2S_{0.78}Se_{0.22}$).

Formation of Ag-Au-Pb mineral assemblage was, probably, the result of interaction of the second model solution with the Au-Ag mineral assemblage of the first stage. According to this model, there form quartz-sericite-feldspar veins with pyrite-sphalerite-galena-

sulfoselenide mineralization (Fig. 10a and b). Owing to the absence of thermodynamic data for imiterite (Ag_2HgS_2), this mineral phase was ignored in the calculation despite its presence in the Ag-Au-Pb mineralized zones. However, the presence of cinnabar in the calculated associations might also suggest the probability of formation of imiterite in these associations.

The ores of low-sulfidation Au-Ag epithermal deposits vary widely: gold-silver-quartz, gold-silver adularia-quartz, gold-silver-telluride, gold-silver-polymetallic and other mineral types of deposits of this group. The formation model of the Rogovik deposit is most likely a modified version of low-sulfidation epithermal type (Cooke and Simmons, 2000; Hedenquist et al., 2000; Marcoux, 1995; Robert et al., 1997, 2007; Sillitoe and Hedenquist, 2003; Pal'yanova, 2008).

The modeling confirmed that boiling and mixing are the most efficient processes, which can lead to the deposition of ore and gangue minerals in epithermal systems (Goryachev and Pirajno, 2014; Hedenquist, 1991; Hedenquist et al., 1996; Karpov et al., 2000, 2001; Moncada et al., 2017; Reed and Spycher, 1984, 1985). Simple cooling of hydrothermal fluids (Drummond and Ohmoto, 1985), dilution by cold groundwater (Hedenquist, 1991; Spycher and Reed, 1989), or interaction with surrounding host rocks (Spycher and Reed, 1989) are likely of lesser importance in the processes of ore deposition.

As the ore-bearing solutions, which formed the mineralization at the early and late stages, we took the fluids, genetically related to diorite

and granite massifs, for which the sources were intermediate magma chambers that differed in composition and depths of formation and which were the derivatives of parental andesite magma (Karpov et al., 2001; Kravtsova, 2010; Kravtsova et al., 2003). This is directly related to the fact that degassing magmas that can be the source for ore substance during the formation of hydrothermal deposits and a large part of silicate melts becomes saturated with the phase of volatiles during the ascent of magma in the crust, which normally leads to the generation of aqueous magmatic fluid (Hedenquist and Lowenstern, 1994).

The Rogovik deposit has much in common with the other OCVB deposits, that have a long period of development and complex composition (Goryachev and Pirajno, 2014; Volkov, 2005). The deposit with similar overlapping of silver-polymetallic stage is a giant Dukat Au-Ag deposit, which occurs in the same trough and is close in the time of formation (Konstantinov et al., 1998, 2003; Kravtsova, 2010). Some more Au-Ag deposits have similar ways of formation: Lunnoe (Ryzhov et al., 2000), Dzhulietta (Palyanova et al., 2016), Kupol (Savva et al., 2012) and others. Examples of similar deposits with Au-Ag and polymetallic mineralizations are also the Apacheta low-sulfidation epithermal Au-Ag (Pb-Zn) deposit (Peru) (Andre-Mayer et al., 2002), Guanajuato (Mexico) (Mango et al., 2013), Waihi (New Zealand) (Brathwaite and Faure, 2002) and Mutnovskoe (Russia, Kamchatka) (Takahashi et al., 2006). The Rogovik gold-silver deposit with Au-Ag and polymetallic mineralization and amalgams of silver and gold in Ag-Au-Pb ores adds to the whole variety of low-sulfidation epithermal Au-Ag deposits. Our study allowed to reveal the main regularities and to specify the interval estimates of the major stages of ore formation in relation to the new types of Au-Ag epithermal deposits, which is the further development of thermodynamic modeling in the study of ore-forming processes (Drummond and Ohmoto, 1985; Reed and Spycher, 1984, 1985; Spycher and Reed, 1989; Simmons and Browne, 2000; Karpov et al., 2001).

7. Conclusions

On the basis of obtained mineralogic-geochemical and microthermometric data and results of modeling we propose the most likely ways for the formation of productive assemblages of different types from the Rogovik deposit (northeastern Russia).

T,X-parameters of the main ore stages were determined using microthermometric results of fluid inclusions. It was established that the formation of Au-Ag mineralization during the early volcanic stage took place at temperature from 300 to 90 °C. An important part in the deposition of Au-Ag ores was played by boiling and degassing processes of the ore-bearing fluid, which is typical for many epithermal Au-Ag deposits. For the Ag-Pb and Ag-Au-Pb mineralization of the late stage we recognized participation of medium-temperature (170–180 °C) solutions with higher concentrations of salts (to 10.5 wt% NaCl-eq.), which during the evolution of the process could be cooled to 120 °C.

The performed thermodynamic modeling of the physicochemical conditions of formation for the Au-Ag mineralization of the Rogovik deposit, carried out within the complex geochemical system K–Na–Ca–Mg–Mn–Al–Si–Ti–Fe–Zn–Cu–Pb–Au–Ag–Hg–S–Se–As–Sb–Cl–C–H–O with the help of the “Selektor-C” software, showed that the reported models (boiling, mixing of ore-bearing gas phase with meteoric water, interaction of aqueous solutions with host rocks and Au-Ag mineralized zones) to a considerable extent describe the compositions of mineral associations of three types of ore mineral assemblages and mechanisms of mineral formation at the studied deposit.

Acknowledgements

This work was supported by grants 16-35-00241 and 17-05-00095 from the Russian Foundation for Basic Research and the state assignment project N 0330-2016-0001. Fluid inclusions study was supported by the Russian Science Foundation, grant № 15-17-20036. The authors

thank Franco Pirajno, Alexander Yakubchuk and the reviewers for their in-depth reviews that considerably improved this manuscript.

References

- Akinfiev, N.N., Tagirov, B.R., 2006. Effect of selenium on silver transport and precipitation by hydrothermal solutions: Thermodynamic description of the Ag-Se-S-Cl-O-H system. *Geol. Ore Deposits* 48 (5), 402–413.
- Akinfiev, N.N., Zotov, A.V., 2001. Thermodynamic description of chloride, hydrosulfide, and hydroxo complexes of Ag(I), Cu(I), and Ag(I) at temperatures of 25–500 °C and pressures of 1–2000 bars. *Geochem. Int.* 39, 990–1006.
- Akinfiev, N.N., Zotov, A.V., 2016. Solubility of chlorargyrite (AgCl_(cr.1.)) in water: New experimental data and a predictive model valid for a wide range of temperatures (273–873 K) and water densities (0.01–1 g·cm⁻³). *Geochim. Cosmochim. Acta* 178, 178–194.
- Andre-Mayer, A.S., Leroy, J.L., Bailly, L., Chauvet, A., Marcoux, E., Grancea, L., Llosa, F., Rosas, J., 2002. Boiling and vertical mineralization zoning: a case study from the Apacheta low-sulfidation epithermal gold-silver deposit, southern Peru. *Miner. Deposita* 37, 452–464.
- Berman, R.G., 1988. Internally-consistent thermodynamic data for minerals in the systems: Na₂O-K₂O-CaO-MgO-FeO-Fe₂O₃-Al₂O₃-SiO₂-TiO₂-H₂O-CO₂. *J. Petrol.* 29, 445–522.
- Bessinger, B., Apps, J.A., 2003. The hydrothermal chemistry of gold, arsenic, antimony, mercury and silver. <http://repositories.cdlib.org/lbnl/LBNL-57395>
- Borisenko, A.S., 1977. Cryometric study of the salt composition of gas-liquid inclusions in minerals. *Geol. Geophys.* 8, 16–27.
- Borisov, M.V., 2000. Geochemical and Thermodynamic Models of Ore-Forming in Hydrothermal Veins. Monograph. Scientific World, Moscow (in Russian).
- Brathwaite, R.L., Faure, K., 2002. The waihi epithermal gold-silver-base metal sulfide-quartz vein system, New Zealand: temperature and salinity controls on electrum and sulfide deposition. *Econ. Geol.* 97, 269–290.
- Breedveld, G.J.F., Prausnitz, J.M., 1973. Thermodynamic properties of supercritical fluids and their mixtures at very high pressure. *AIChE J.* 19, 783–796.
- Brown, P.E., 1989. FLINCOR: A microcomputer program for the reduction and investigation of fluid-inclusion data. *Am. Mineral.* 74, 1390–1393.
- Chudnenko, K.V., 2010. Thermodynamic Modeling in Geochemistry: Theory, Algorithms, Software, Applications. Academic Publishing House Geo, Novosibirsk (in Russian).
- Chudnenko, K., Pal'yanova, G., 2013. Thermodynamic properties of Ag–Au–Hg solid solutions. *Thermochim. Acta* 572, 65–70.
- Chudnenko, K.V., Palyanova, G.A., 2016. Thermodynamic modeling of native formation of Au-Ag-Cu-Hg solid solutions. *Appl. Geochem.* 66, 88–100.
- Chudnenko, K.V., Pal'yanova, G.A., Anisimova, G.S., Moskvitin, S.G., 2015. Physicochemical modeling of formation of Ag-Au-Hg solid solutions: Kyuchyus deposit (Yakutia, Russia) as an example. *Appl. Geochem.* 55, 138–151.
- Cooke, D., Simmons, S., 2000. Characteristics and Genesis of epithermal gold deposits. *SEG Rev.* 13, 221–244.
- Diakonov, I., Pokrovski, G., Schott, J., Castet, S., Gout, R., 1996. An experimental and computational study of sodium–aluminum complexing in crustal fluids. *Geochim. Cosmochim. Acta* 60, 197–211.
- Diemar, G.A., 2008. Supergene Dispersion of Antimony and a Geochemical Exploration Model for Antimony Ore Deposits (Ph.D. Dissertation). University of Western Sydney, Australia.
- Drummond, E., Ohmoto, H., 1985. Chemical evolution and mineral deposition in boiling hydrothermal systems. *Econ. Geol.* 80, 126–147.
- Frezzotti, M.L., Tecce, F., Casagli, A., 2012. Raman spectroscopy for fluid inclusion analysis. *J. Geochem. Explor.* 112, 1–20.
- Fujita, T., Taguchi, R., Kubo, H., Shibata, E., Nakamura, T., 2009. Immobilization of arsenic from novel synthesized scorodite – analysis on solubility and stability. *Mater. Trans.* 50, 321–331.
- Gamyranin, G.N., Goryachev, N.A., Bortnikov, N.S., Anikina, E.Yu., 2003. Types of silver mineralization in Verkhoyansk-Kolyma mesozoides (geology, mineralogy, genesis, and metallogeny). *Tikhookeanskaya Geol.* 22 (6), 113–126 (in Russian).
- Goryachev, N.A., Pirajno, F., 2014. Gold deposits and gold metallogeny of Far East Russia. *Ore Geol. Rev.* 59, 123–151.
- Haar, L., Gallagher, J.S., Kell, G.S., 1984. NBS/NRC Steam tables. Thermodynamic and transport properties and computer programs for vapor and liquid of water in SI units. Mc Graw-Hill, New York.
- Hedenquist, J.W., 1991. Boiling and dilution in the shallow portion of the Waiotapu geothermal system, New-Zealand. *Geochim. Cosmochim. Acta* 55, 2753–2765.
- Hedenquist, J.W., Lowenstern, J.R., 1994. The role of magmas in the formation of hydrothermal ore deposits. *Nat. Internat. Weekly J. Sci.* 370 (6), 519–527.
- Hedenquist, J.W., Izawa, E., Arribas, A., White, N.C., 1996. Epithermal gold deposits: Styles, characteristics, and exploration. *Resour. Geol. Spec. Publ.* 1 18 p.
- Hedenquist, J.W., Arribas, A., Gonzalez-Urien, E., 2000. Exploration for epithermal gold deposits. *SEG Rev.* 7 (13), 245–277.
- Helgeson, H.C., Delany, J.M., Nesbitt, H.W., Bird, D.K., 1978. Summary and critique of the thermodynamic properties of rock-forming minerals. *Am. J. Sci.* 278A, 1–229.
- Holland, T.J.B., Powell, R., 1998. An internally consistent thermodynamic dataset for phases of petrological interest. *J. Metamorph. Geol.* 16, 309–343.
- Holland, T.J.B., Powell, R., 2003. Activity-composition relations for phases in petrological calculations: an asymmetric multicomponent formulation. *Contrib. Mineral. Petrol.* 145, 492–501.
- Holland, T.J.B., Baker, J.M., Powell, R., 1998. Mixing properties and activity-composition relationships of chlorites in the system MgO-FeO-Al₂O₃-SiO₂-H₂O. *Eur. J. Mineral.*

- 10, 395–406.
- Hurtig, N.C., Williams-Jones, A.E., 2014. An experimental study of the transport of gold through hydration of AuCl in aqueous vapor and vapor-like fluids. *Geochim. Cosmochim. Acta* 127, 305–325.
- Hurtig, N.C., Williams-Jones, A.E., 2015. Porphyry-epithermal Au-Ag-Mo ore formation by vapor-like fluids: New insights from geochemical modeling. *Geology* 43 (7), 587–590.
- Johnson, J.W., Oelkers, E.H., Helgeson, H.C., 1992. SUPCRT92: software package for calculating the standard molal thermodynamic properties of mineral, gases, aqueous species, and reactions from 1 to 5000 bars and 0 to 1000 °C. *Comput. Geosci.* 18, 899–947.
- Kalinin, A.I., Yarantseva, L.M., Natalenko, V.E., Kanishchev, V.K., 1984. Geology of silver-complex-metal mineralization of the Novyi Dzhagyn intrusive arched structure. *Kolyma* 1, 29–31 (in Russian).
- Karpov, I.K., Chudnenko, K.V., Kulik, D.A., 1997. Modeling chemical mass-transfer in geochemical processes: thermodynamic relations, conditions of equilibria and numerical algorithms. *Am. J. Sci.* 297, 767–806.
- Karpov, I.K., Kravtsova, R.G., Chudnenko, K.V., Artimenko, M.V., 2000. A physico-chemical model for the volcanic hydrothermal ore-forming system of epithermal gold-silver deposits, Northeastern Russia. *J. Geochem. Explor.* 69–70, 323–325.
- Karpov, I.K., Chudnenko, K.V., Kravtsova, R.G., Bychinskiy, V.A., 2001. Simulation modeling of physical and chemical processes of dissolution, transport and deposition of gold in epithermal gold-silver deposits of the North-East Russia. *Geol. Geophys.* 3, 393–408.
- Karpov, I.K., Chudnenko, K.V., Kulik, D.A., Bychinskii, V.A., 2002. The convex programming minimization of five thermodynamic potentials other than Gibbs energy in geochemical modeling. *Am. J. Sci.* 302 (4), 281–311.
- Konstantinov, M.M., Natalenko, V.E., Kalinin, A.I., Struzhkov, S.F., 1998. The Dukat Gold-Silver Deposit. Nedra, Moscow (in Russian).
- Konstantinov, M.M., Kostin, A.V., Sidorov, A.A., 2003. Geology of Silver Deposits. *Sakhapolografizdat, Yakutsk* (in Russian).
- Kostin, A.V., Denisov, G.V., 2007. Large noble metal ore-magmatic systems of the Western Verkhoyansk region. *Otechestvennaya Geol.* 5, 17–25 (in Russian).
- Kostin, A.V., Okunev, A.E., Denisov, G.V., Osipov, L.V., 2011. Characteristic features of silver mineralization in the Nizhneimnek and Allara-Sakh ore clusters. *Otechestvennaya Geol.* 5, 3–10 (in Russian).
- Kravtsova, R.G., 2010. Geochemistry and conditions of forming gold-silver ore-forming systems, Northern Okhotsk Region. Academic Publishing House “Geo”, Novosibirsk (in Russian).
- Kravtsova, R.G., Zakharov, M.N., Shatkov, N.G., 1998. Mineralogical and geochemical features of host rocks of the Goltsovoe silver-base metal deposit (Northeastern Russia). *Geol. Ore Deposits* 40 (3), 197–210.
- Kravtsova, R.G., Borovikov, A.A., Borisenko, A.S., Prokof'ev, V.Yu., 2003. Formation conditions of gold-silver deposits in the northern Okhotsk Region, Russia. *Geol. Ore Deposits* 45 (5), 395–415.
- Kravtsova, R.G., Makshakov, A.S., Tarasova, Yu.I., Kulikova, Z.I., 2012. Mineralogical and geochemical features of the host rocks and ores of the Rogovik gold-silver deposit (northeastern Russia). *Izv. SO RAEN. Ser. Nauki o Zemle. Geologiya, Poiski i Razvedka Rudnykh Mestorozhdenii* 41 (2), 11–22 (in Russian).
- Kravtsova, R.G., Makshakov, A.S., Pavlova, L.A., 2015. Mineral and geochemical compositions, regularities of distribution, and specific formation of ore mineralization of the Rogovik gold-silver deposit (northeastern Russia). *Russ. Geol. Geophys.* 56 (10), 1367–1383.
- Krylova, V.V., Kichigin, L.N., 1989. Silver amalgams as the main silver-bearing minerals of quartz-carbonate veins of the Eastern Verkhoyansk. *TsNIGRI, Moscow*, vol. 239, pp. 89–90 (in Russian).
- Kuznetsov, V.M., Livach, A.E., 2005. Structure and metallogenic zoning of the Balygchan-Sugoi trough. In: *Problems of Metallogeny of the Ore Districts of Northeastern Russia*. SVKNII DVO RAN, Magadan, pp. 156–176 (in Russian).
- Kuznetsov, V.M., Palymyskaya, Z.A., Puzryev, V.P., Pchelintseva, R.Z., Stepanov, V.A., Shchitova, V.I., 1992. Gold-silver mineralization in a cryptovolcanic structure. *Kolyma* 3, 5–8 (in Russian).
- Lee, B.I., Kesler, M.G., 1975. Generalized thermodynamic correlation based on three-parameter corresponding states. *AIChE J.* 21, 510–527.
- Mango, H., Arehart, G., Oreskes, N., Zantop, H., 2013. Origin of epithermal Ag-Au-Cu-Pb-Zn mineralization in Guanajuato, Mexico. *Miner. Deposita* 49 (1), 119–143.
- Marcoux, E., 1995. Gold and volcanoes: epithermal gold deposits, a review. *C.R. Acad. Sci. Paris.* 321, 723–735.
- Marini, L., Accornero, M., 2012. Prediction of the thermodynamic properties of meta-arsenate and metal-arsenate aqueous complexes to high temperatures and pressures and some geological consequences. *Environ. Geol.* 52, 1343–1363.
- Moncada, D., Baker, D., Bodnar, R.J., 2017. Mineralogical, petrographic and fluid inclusion evidence for the link between boiling and epithermal Ag-Au mineralization in the La Luz area, Guanajuato Mining District, México. *Ore Geol. Rev.* 89, 143–170.
- Naumov, G.B., Ryzhenko, B.N., Khodakovskiy, I.L., 1974. *Handbook of Thermodynamic Data*. NTIS, Springfield, VA, USA.
- Pal'yanova, G.A., Kolonin, G.R., 2007. Geochemical mobility of Au and Ag during hydrothermal transfer and precipitation: thermodynamic simulation. *Geochem. Int.* 45 (8), 744–757.
- Pal'yanova, G., 2008. Physicochemical modeling of the coupled behavior of gold and silver in hydrothermal processes: gold fineness, Au/Ag ratio and their possible implications. *Chem. Geol.* 255, 399–413.
- Pal'yanova, G.A., Chudnenko, K.V., Zhuravkova, T.V., 2014. Thermodynamic properties of solid solutions in the Ag₂S–Ag₂Se system. *Thermochim. Acta* 575, 90–96.
- Pal'yanova, G.A., Kravtsova, R.G., Zhuravkova, T.V., 2015. Ag₂(S,Se) solid solutions in the ores of the Rogovik gold-silver deposit (northeastern Russia). *Russ. Geol. Geophys.* 56 (12), 1738–1748.
- Pal'yanova, G.A., Savva, N.E., Zhuravkova, T.V., Kolova, E.E., 2016. Gold and silver minerals in low-sulfide ores of the Dzhulietta deposit (northeastern Russia). *Russ. Geol. Geophys.* 57 (8), 1171–1190.
- Perfetti, E., Pokrovskii, G.S., Ballerat-Busserolles, K., Majer, V., Gibert, F., 2008. Densities and heat capacities of aqueous arsenious and arsenic acid solutions to 350 °C and 300 bar, and revised thermodynamic properties of As(OH)_{3(aq)}, AsO(OH)_{3(aq)} and iron sulfarsenide minerals. *Geochim. Cosmochim. Acta* 72, 713–731.
- Plyashkevich, A.A., 2002. *Mineralogy and Geochemistry of Tin-Silver-Polymetallic Deposits of the North-East of Russia*. SVKNII DVO RAN, Magadan (in Russian).
- Pokrovskii, V.A., Helgeson, H.C., 1995. Thermodynamic properties of aqueous species and the solubilities of minerals at high pressures and temperatures: the system Al₂O₃–H₂O–NaCl. *Am. J. Sci.* 295, 1255–1342.
- Pokrovskii, G., Gout, R., Schott, J., Zotov, A., Harrichoury, J.-C., 1996. Thermodynamic properties and stoichiometry of As (III) hydroxide complexes at hydrothermal conditions. *Geochim. Cosmochim. Acta* 60, 737–749.
- Reed, M.H., Spycher, N.F., 1984. Calculation of high temperature pH and mineral equilibria in hydrothermal waters, with application to geothermometry and studies of boiling and dilution. *Geochim. Cosmochim. Acta* 48, 1479–1492.
- Reed, M.H., Spycher, N.F., 1985. Boiling, cooling and oxidation in epithermal systems: a numerical modeling approach. *Rev. Econ. Geol.* 2, 249–272.
- Reid, R.C., Prausnitz, J.M., Sherwood, T.K., 1977. *The Properties of Gases and Liquids*. McGraw-Hill Book Company, New York.
- Robert, F., Poulsen, K.H., Dube, B., 1997. Gold Deposits and Their Geological Classification. In: “Proceedings of Exploration 97: Fourth Decennial International Conference on Mineral Exploration” edited by A.G. Gubins, pp. 209–220.
- Robert, F., Brommecker, R., Bourne, B.T., Dobak, P.J., McEwan, C.J., Rowe, R.R., Zhou, X., 2007. Models and Exploration Methods for Major Gold Deposit Types. In: “Proceedings of Exploration 07: Fifth Decennial International Conference on Mineral Exploration” edited by B. Milkereit, pp. 691–711.
- Robie, R.A., Hemingway, B.S., 1995. Thermodynamic properties of minerals and related substances of 298.15 K and 1 bar pressure and at higher temperatures. *U.S. Geol. Surv. Bull.*, 2113, Government Printing Office, Washington.
- Roedder, E., 1984. Fluid inclusions. *Miner. Soc. Amer., Rev. Miner.* 12, 644.
- Ryzhov, O.B., Struzhkov, S.F., Aristov, V.V., Dvurechenskaya, S.S., Ostapenko, L.A., Sandomirskaya, S.M., Zaitsev, V.I., Korzh, V.D., 2000. The Lunnyi gold-silver deposit (northeast Russia): geological setting and mineral composition of ores. *Geol. Ore Deposits* 42 (4), 277–295.
- Saunders, J.A., Unger, D.L., Kamenov, G.D., Fayek, M., Hames, W.E., Utterback, W.C., 2008. Genesis of Middle Miocene Yellowstone-hotspot related bonanza epithermal Au-Ag deposits, Northern Great Basin Region, USA. *Miner. Deposita* 43, 715–734.
- Savva, N.E., Pal'yanova, G.A., Byankin, M.A., 2012. The problem of genesis of gold and silver sulfides and selenides in the Kupol deposit (Chukot Peninsula, Russia). *Russ. Geol. Geophys.* 53 (5), 457–466.
- Seal, R.R., Essene, E.J., Kelly, W.C., 1990. Tetrahydroite and tennantite; evaluation of thermodynamic data and phase equilibria. *Can. Mineral.* 28, 725–738.
- Shock, E.L., Helgeson, H.C., Sverjensky, D.A., 1989. Calculation of the thermodynamic and transport properties of aqueous species at high pressures and temperatures: standard partial molal properties of inorganic neutral species. *Geochim. Cosmochim. Acta* 53, 2157–2183.
- Shock, E.L., Sassani, D.C., Willis, M., Sverjensky, D.A., 1997. Inorganic species in geologic fluids: correlation among standard molal thermodynamic properties of aqueous ions and hydroxide complexes. *Geochim. Cosmochim. Acta* 61, 907–950.
- Shpikerman, V.I., Goryachev, N.A., 1996. Plate tectonics metallogeny of fold systems of accretion type // *Metallogeny of fold systems from the positions of plate tectonics. Ural Branch, RAS, Ekaterinburg*, pp. 64–78 (in Russian).
- Sidorov, A.A., 1987. Ore Formation of Phanerozoic Provinces (Northern Part of the Pacific Rim). SVKNII DVO AN SSSR, Magadan (in Russian).
- Sidorov, A.A., Volkov, A.V., Belyi, V.F., Alekseev, V.Yu., Kolova, E.E., 2009. The gold-silver Okhotsk-Chukotka volcanic belt. *Geol. Ore Deposits* 51 (6), 441–455.
- Sillitoe, R.H., Hedenquist, J.W., 2003. Linkages between volcanotectonic settings, ore-fluid compositions, and epithermal precious metal deposits. *Soc. Econ. Geol., Spec. Publ.* 10, 315–343.
- Simmons, S.F., Browne, P.R.L., 2000. Hydrothermal minerals and precious metals in the Broadlands-Ohaaki geothermal system: implications for understanding low-sulfidation epithermal environments. *Econ. Geol.* 95, 971–999.
- Spycher, N.F., Reed, M.H., 1989. Evolution of a Broadlands-type epithermal ore fluid along alternative P-T paths: implications for the transport and deposition of base, precious and volatile metals. *Econ. Geol.* 84, 328–359.
- Steele-MacInnis, M., Bondar, R.J., Naden, J., 2011. Numerical model to determine the composition of H₂O–NaCl–CaCl₂ fluid inclusions based on microthermometric and microanalytical data. *Geochim. Cosmochim. Acta* 75, 21–40.
- Sverjensky, D.A., Shock, E.L., Helgeson, H.C., 1997. Prediction of the thermodynamic properties of aqueous metal complexes to 1000°C and 5 kb. *Geochim. Cosmochim. Acta* 61, 1359–1412.
- Tagirov, B.R., Baranova, N.N., Zotov, A.V., Schott, J., Bannykh, L.N., 2006. Experimental determination of the stabilities of Au₂S(cr) at 25 °C and Au(HS)₂⁻ at 25–250 °C. *Geochim. Cosmochim. Acta* 70, 3689–3701.
- Takahashi, R., Matsueda, H., Okrugin, V.M., Ono, Sh., 2006. Polymetallic and Au-Ag Mineralizations at the Mutnovskoe Deposit in South Kamchatka, Russia. *Resour. Geol.* 56 (2), 141–156.
- Tanger, J.C., Helgeson, H.C., 1988. Calculation of the thermodynamic and transport properties of aqueous species at high pressures and temperatures: revised equations of state for standard partial molal properties of ions and electrolytes. *Am. J. Sci.* 288, 19–98.
- Volkov, A.V., 2005. The distribution and formation conditions of gold deposits in tectono-

- magmatic activation zones of the Northeast of Russia. *Geol. Ore Deposits* 47 (3), 188–205.
- Walas, S.M., 1985. *Phase Equilibria in Chemical Engineering*. Butterworth Publ, Boston.
- White, N.C., Hedenquist, J.W., 1990. Epithermal environments and styles of mineralization: variations and their causes, and guidelines for exploration. *J. Geochem. Explor.* 36, 445–474.
- Williams-Jones, A., Normand, C., 1997. Control of mineral parageneses in the system Fe–Sb–S–O. *Econ. Geol.* 92, 308–324.
- Yokokawa, H., 1988. Tables of thermodynamic properties of inorganic compounds. *Journal of the national chemical laboratory for industry*. Tsukuba Ibaraki 305, Japan, 83, 27–118.
- Zhuravkova, T.V., Palyanova, G.A., Kravtsova, R.G., 2015. Physicochemical formation conditions of silver sulfoselenides at the Rogovik deposit, northeastern Russia. *Geol. Ore Deposits* 57 (4), 313–330.
- Zotov, A.V., Shikina, N.D., Akinfiev, N.N., 2003. Thermodynamic properties of the Sb(III) hydroxide complex $\text{Sb}(\text{OH})_{3(\text{aq})}$ at hydrothermal conditions. *Geochim. Cosmochim. Acta* 67, 1821–1836.